Article

Host metabolism balances microbial regulation of bile acid signalling

https://doi.org/10.1038/s41586-024-08379-9

Received: 31 December 2022

Accepted: 8 November 2024

Published online: 08 January 2025

Check for updates

Tae Hyung Won[1,10,12], Mohammad Arifuzzaman[2,3,12], Christopher N. Parkhurst[2,12], Isabella C. Miranda[2], Bingsen Zhang[1], Elin Hu[2,3], Sanchita Kashyap[2,3], Jeffrey Letourneau[4], Wen-Bing Jin[2], Yousi Fu[5], Douglas V. Guzior[5,6], JRI Live Cell Bank*, Robert A. Quinn[5], Chun-Jun Guo[2,3,7], Lawrence A. David[4,8], David Artis[2,3,7,9]✉ & Frank C. Schroeder[1]✉

Metabolites derived from the intestinal microbiota, including bile acids (BA), extensively modulate vertebrate physiology, including development[1], metabolism[2–4], immune responses[5–7] and cognitive function[8]. However, to what extent host responses balance the physiological effects of microbiota-derived metabolites remains unclear[9,10]. Here, using untargeted metabolomics of mouse tissues, we identified a family of BA–methylcysteamine (BA–MCY) conjugates that are abundant in the intestine and dependent on vanin 1 (VNN1), a pantetheinase highly expressed in intestinal tissues. This host-dependent MCY conjugation inverts BA function in the hepatobiliary system. Whereas microbiota-derived free BAs function as agonists of the farnesoid X receptor (FXR) and negatively regulate BA production, BA–MCYs act as potent antagonists of FXR and promote expression of BA biosynthesis genes in vivo. Supplementation with stable-isotope-labelled BA–MCY increased BA production in an FXR-dependent manner, and BA–MCY supplementation in a mouse model of hypercholesteraemia decreased lipid accumulation in the liver, consistent with BA–MCYs acting as intestinal FXR antagonists. The levels of BA–MCY were reduced in microbiota-deficient mice and restored by transplantation of human faecal microbiota. Dietary intervention with inulin fibre further increased levels of both free BAs and BA–MCY levels, indicating that BA–MCY production by the host is regulated by levels of microbiota-derived free BAs. We further show that diverse BA–MCYs are also present in human serum. Together, our results indicate that BA–MCY conjugation by the host balances host-dependent and microbiota-dependent metabolic pathways that regulate FXR-dependent physiology.

Vertebrates have diverse communities of bacteria, protozoa, fungi and viruses, collectively referred to as the microbiota. Co-evolution with these microorganisms has resulted in the establishment of host–microbiota crosstalk via complex metabolic networks[9–11]. One such example is the metabolism of BAs[2–4,12,13], which have a central role in vertebrate physiology as ligands of FXR, a conserved nuclear hormone receptor that controls cholesterol and BA biosynthesis, as well as fat metabolism and glucose homeostasis[3,4,14–16]. BAs are produced in the liver where they are conjugated to taurine and amino acids by BA-coenzyme A (CoA):amino acid *N*-acyltransferase (BAAT)[17,18]. Conjugated BAs are then secreted via the biliary system into the intestine where they undergo extensive modification by microbial metabolism[4,19–23], including diverse dehydroxylation and oxidation reactions as well as deconjugation, which recovers free, unconjugated BAs that are efficiently reabsorbed and transported back to the liver. Although BA–taurine conjugates are inactive or have weak agonistic or antagonistic activities[24–27], free BAs act as potent FXR agonists that negatively regulate BA production[2,3,14,28]. BA–taurine conjugation by the host and microbial deconjugation thus form a negative-feedback loop that tightly regulates BA levels and BA-dependent physiology. However, the requirement for adaptation to changing metabolic demands and feeding states and the ubiquity of feed-forward signalling in biological systems[29] raises the question whether there exist FXR antagonists that act as positive regulators of BA production. Here we utilized untargeted metabolomics to compare germ-free and microbiota-replete specific pathogen-free (SPF) mice to uncover a host-mediated BA modification

[1]Department of Chemistry and Chemical Biology, Boyce Thompson Institute, Cornell University, Ithaca, NY, USA. [2]Joan and Sanford I. Weill Department of Medicine, Jill Roberts Institute for Research in Inflammatory Bowel Disease, Division of Gastroenterology and Hepatology, Weill Cornell Medicine, Cornell University, New York, NY, USA. [3]Friedman Center for Nutrition and Inflammation, Weill Cornell Medicine, Cornell University, New York, NY, USA. [4]Department of Molecular Genetics and Microbiology, Duke University, Durham, NC, USA. [5]Department of Biochemistry and Molecular Biology, Michigan State University, East Lansing, MI, USA. [6]Department of Microbiology, Genetics, and Immunology, Michigan State University, East Lansing, MI, USA. [7]Department of Microbiology and Immunology, Weill Cornell Medicine, Cornell University, New York, NY, USA. [8]Program in Computational Biology and Bioinformatics, Duke University School of Medicine, Durham, NC, USA. [9]Allen Discovery Center for Neuroimmune Interactions, Weill Cornell Medicine, Cornell University, New York, NY, USA. [10]Present address: College of Pharmacy and Institute of Pharmaceutical Sciences, CHA University, Pocheon-si, Republic of Korea. [12]These authors contributed equally: Tae Hyung Won, Mohammad Arifuzzaman, Christopher N. Parkhurst. *A list of authors and their affiliations appears at the end of the paper. ✉e-mail: dartis@med.cornell.edu; schroeder@cornell.edu

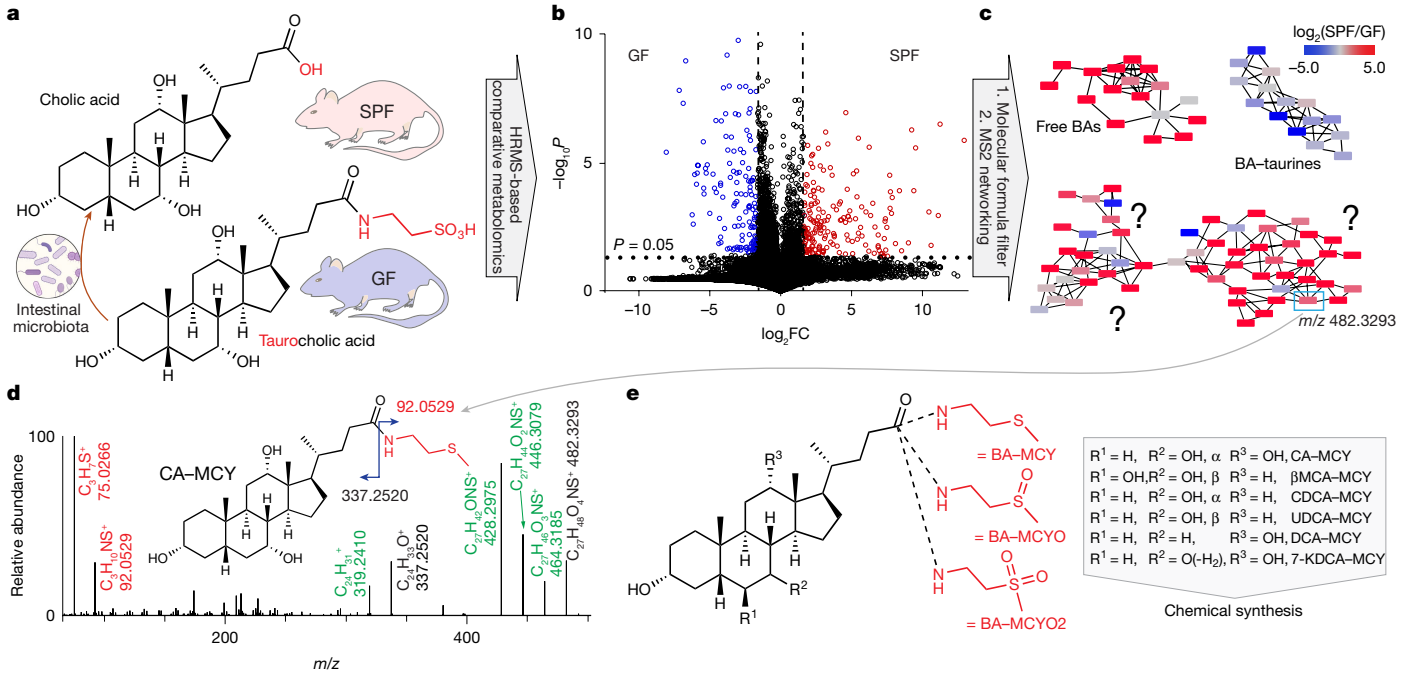

Fig. 1 | Identification of MCY conjugates of BAs. a, Primary role of gut microbiota in BA metabolism, and schematic overview of the analytical strategy for comparison of germ-free (GF) and SPF mice. **b**, Volcano plots of differential metabolites detected in serum of germ-free ($n = 12$) and SPF ($n = 9$) mice. The blue and red dots represent metabolites fivefold or more-fold downregulated or upregulated in germ-free relative to SPF mice at $P < 0.05$, as calculated by unpaired two-sided Student's *t*-test. FC, fold change. **c**, Partial representation of the MS2 networks (cosine > 0.7) for mouse serum obtained in positive-ion electrospray ionization (ESI^+) and negative-ion electrospray ionization (ESI^-) modes, showing clusters representing free BAs, BA–taurine conjugates and previously unannotated BA–MCY conjugates. The red and blue nodes are downregulated and upregulated, respectively, in serum of germ-free compared with SPF mice. See Supplementary Figs. 1–3 for full MS2 networks, including *m/z* values for all nodes. **d**, MS2 spectrum of CA–MCY. The red MS2 fragments represent the MCY group; the green MS2 fragments are derived from water loss. **e**, Structures of BA–MCY conjugates identified in mouse serum. The schematics in panel **a** were created using BioRender (https://biorender.com).

generating potent FXR antagonists that act as intestinal regulators of BA metabolism.

Comparative metabolomics reveals BA–MCYs

Lack of microbial deconjugation results in increased levels of BA–taurine conjugates in germ-free mice, whereas abundances of free BAs are dramatically reduced[24]. We hypothesized that abundances of yet unannotated BA derivatives may be similarly affected by the absence of the microbiota. To discover such unannotated compounds, we first obtained a comprehensive overview of microbiota-dependent changes in the mouse serum metabolome via high-resolution mass spectrometry (HRMS)-based comparative metabolomics of samples from microbiota-replete SPF and germ-free mice (Fig. 1a). The resulting datasets were processed using the xcms-based[30] Metaboseek platform[31], which facilitates identification of mass spectrometry features whose abundances differ significantly between different conditions (Fig. 1b). This untargeted comparison revealed stark differences between germ-free and SPF mice. In total, we detected more than 40,000 mass spectrometry features from combined analyses of serum samples in positive and negative ionization modes, of which approximately 10% were significantly differential (at $P \leq 0.05$) between germ-free and SPF mice. To prioritize among the large number of differential features, we focused on compounds that were robustly detected in all replicates (see Methods) and at least fivefold different in germ-free relative to SPF samples. Using these stringent criteria, we detected several hundred microbiota-dependent metabolites in the serum metabolome (Supplementary Table 1). For further characterization, we acquired tandem mass spectrometry (MS2) data for all differential metabolites. To focus on BAs and BA derivatives, we applied a permissive molecular formula filter that required the presence of MS2 fragments containing a complete 24-carbon backbone, which would suggest the presence of a steroid backbone (see Methods). MS2 networking revealed three major clusters of microbiota-dependent metabolites with fragmentation patterns, indicating that they represent BAs or BA derivatives (Fig. 1c and Supplementary Figs. 1–3). Two of these clusters represented BA–taurine conjugates and free BAs, whose abundances were greatly increased and decreased in germ-free mice, respectively, as expected, given the lack of microbial taurine deconjugation. By contrast, the third cluster appeared to represent a family of previously unannotated BA derivatives, whose abundances, similar to free BAs, were reduced in germ-free mice.

Detailed analysis of the mass spectrometry isotope patterns and MS2 spectra of the putative BA derivatives suggested the presence of an MCY moiety (Fig. 1d and Extended Data Fig. 1). The MS2 spectra further indicated that these MCY derivatives belong to three different series, representing putative BA–MCYs, corresponding sulfoxides (BA–MCYO) and sulfodioxides (BA–MCYO2; Extended Data Fig. 1). Structures of these BA–MCYs were proposed based on the relative abundances and retention times of free BAs in the analysed samples and confirmed via synthesis of authentic standards, which led to the identification of a total of 18 BA derivatives, including the MCY, MCYO and MCYO2 derivatives of cholic acid, β-muricholic acid (βMCA), chenodeoxycholic acid (CDCA), ursodeoxycholic acid (UDCA), deoxycholic acid (DCA) and 7-ketodeoxycholic acid (7-KDCA; Fig. 1e, Supplementary Table 2 and Supplementary Fig. 4; see Supplementary information for synthetic procedures and NMR data). Together, our untargeted metabolomic comparison of SPF and germ-free mice revealed BA–MCYs as a previously unannotated family of microbiota-dependent BA derivatives.

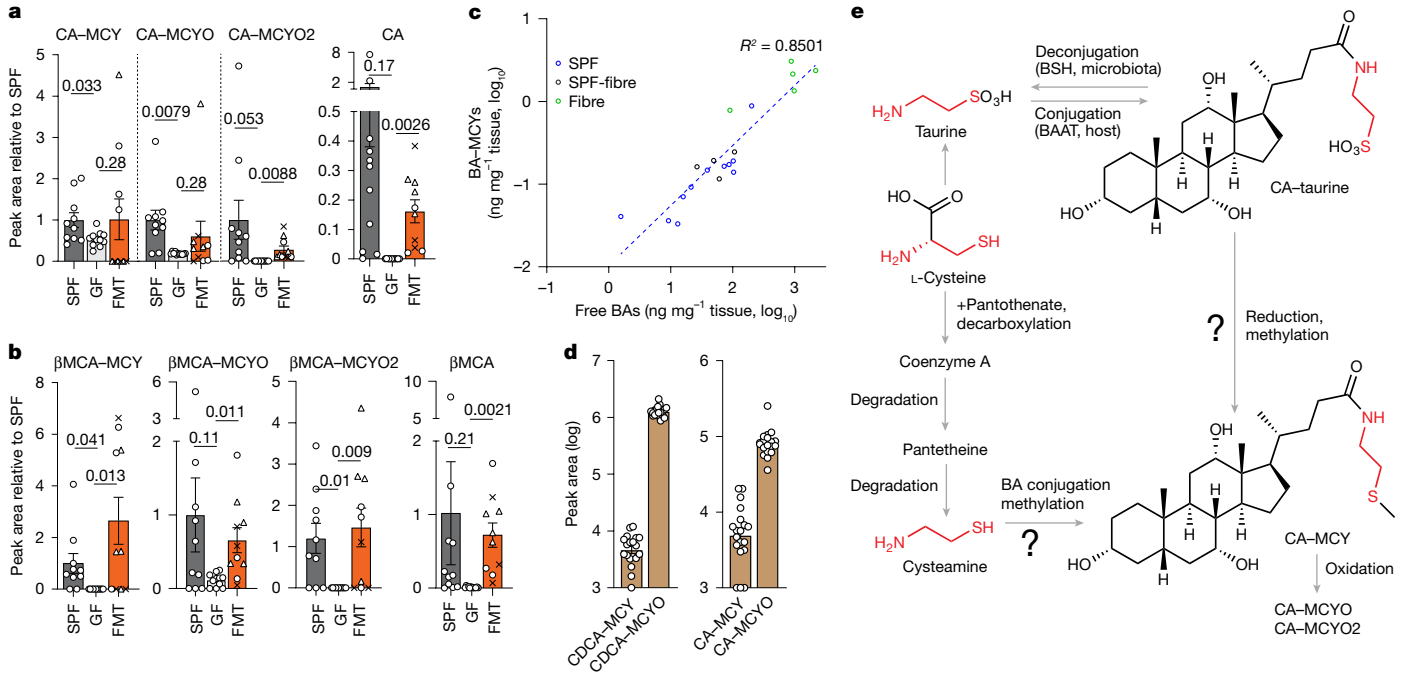

Fig. 2 | Microbiota dependence and biosynthesis of BA–MCY conjugates. **a**,**b**, Relative abundances of CA–MCY conjugates (**a**) and βMCA–MCY conjugates (**b**), as well as corresponding free BAs in the serum of SPF mice ($n = 11$), germ-free mice ($n = 12$) and mice that received FMT ($n = 10$; the three donors are represented by triangles, circles and crosses, $n = 3$–4 for each donor). Data are shown as mean ± s.e.m. *P* values were calculated using unpaired two-sided Student's *t*-test with Welch's correction. **c**, Relationship between abundances of free BAs and BA–MCY conjugates in the liver of SPF mice ($n = 11$), SPF control mice for the inulin fibre diet study ($n = 4$) and inulin fibre diet-fed SPF mice ($n = 5$). **d**, Relative abundance of CA–MCY conjugates or CDCA–MCY conjugates in human serum ($n = 19$). Data are shown as mean ± s.e.m. **e**, Pathways considered for the origin of BA–MCY conjugates. MCY conjugates could originate either from reduction of BA–taurine conjugates produced by the liver enzyme BAAT or conjugation of BAs with cysteamine or another cysteamine derivative from CoA and pantetheine degradation. Oxidation of MCY conjugates produces the corresponding MCYO and MCYO2 conjugates.

Microbiota dependence of BA–MCY levels

Abundances of BA–MCYs were strongly reduced in germ-free compared with SPF serum samples, but not abolished (Fig. 2a,b, Extended Data Fig. 2a and Supplementary Table 3). Similarly, BA–MCY levels were decreased in faeces of germ-free mice compared with SPF mice (Extended Data Fig. 2b–d). To better understand the relationship between BA–MCY levels and the presence of the microbiota, we next tested whether introduction of human microbiota into germ-free mice would affect BA–MCY production. For this purpose, we performed human faecal microbiota transplantation (FMT) from healthy individuals into germ-free mice[32], and then profiled BAs and BA conjugates in serum and faeces. We found that abundances of both free BAs and BA–MCY conjugates were greatly increased in serum and faeces of mice that received human FMT (Fig. 2a,b and Extended Data Fig. 2a–g).

The results from our comparison of germ-free with SPF and human FMT mice suggested that BA–MCY levels are governed in part by levels of the corresponding free BAs. In previous work, we and others have shown that changes in the microbiota induced by supplementation with inulin fibre can dramatically increase levels of free BAs in the serum of SPF mice[32,33]. We took advantage of this to test whether such a dietary intervention-based increase of free BA levels would also affect BA–MCY levels. We observed that BA–MCY levels were greatly increased in SPF mice fed an inulin-based high-fibre diet (Extended Data Fig. 3a–c), suggesting that expansion of the free BA pool leads to increased BA conjugation with MCY. Moreover, we found that levels of free BAs and BA–MCY conjugates in SPF mice fed different diets are generally correlated (Fig. 2c and Extended Data Fig. 3d,e). Finally, to determine whether BA–MCYs are also present in humans, we analysed human serum samples, which revealed MCY derivatives of all major BAs common in humans (Fig. 2d and Extended Data Fig. 3f,g). Collectively, these data indicate that BA–MCY conjugates are present in mouse and human, and that increases of free BA levels, following human FMT into germ-free mice or as a result of supplementation with dietary fibre, are associated with parallel increases of the corresponding BA–MCY conjugates.

Biochemical origin of BA–MCY conjugates

To further clarify the roles of host and microbiota for the production of the BA–MCY conjugates, we next investigated the in vivo origin of the cysteamine moiety. Cysteamine is produced primarily via degradation of CoA[34], and oxidation of cysteamine in the liver and other tissues produces taurine, which is then conjugated with BAs in the liver, producing BA–taurine conjugates that are secreted into the intestine. Therefore, we considered two different models for the origin of the MCY moieties in the BA–MCYs (Fig. 2e). First, these compounds could originate from conjugation of BAs with cysteamine or a cysteamine derivative derived from breakdown of CoA. Alternatively, the BA–MCY conjugates could be derived from reduction of corresponding BA–taurine derivatives by the host or the gut microbiota (Fig. 2e). To distinguish between these scenarios, we performed a series of stable-isotope labelling experiments with taurine-d_4 and L-cysteine-3,3-d_2 in SPF mice (Extended Data Fig. 4a–c). High-performance liquid chromatography (HPLC)–HRMS analysis of serum from SPF mice supplemented with taurine-d_4 revealed extensive labelling of taurine conjugates of BAs, as expected (Extended Data Fig. 4a). However, none of the MCY conjugates were labelled (Extended Data Fig. 4a), indicating that the biosynthetic pathways of taurine and MCY conjugates are distinct. Next, to test whether the MCY conjugates originate from incorporation of a cysteine-derived cysteamine moiety, we analysed serum samples from SPF mice supplemented with L-cysteine-3,3-d_2 (Extended Data Fig. 4b,c). HPLC–HRMS

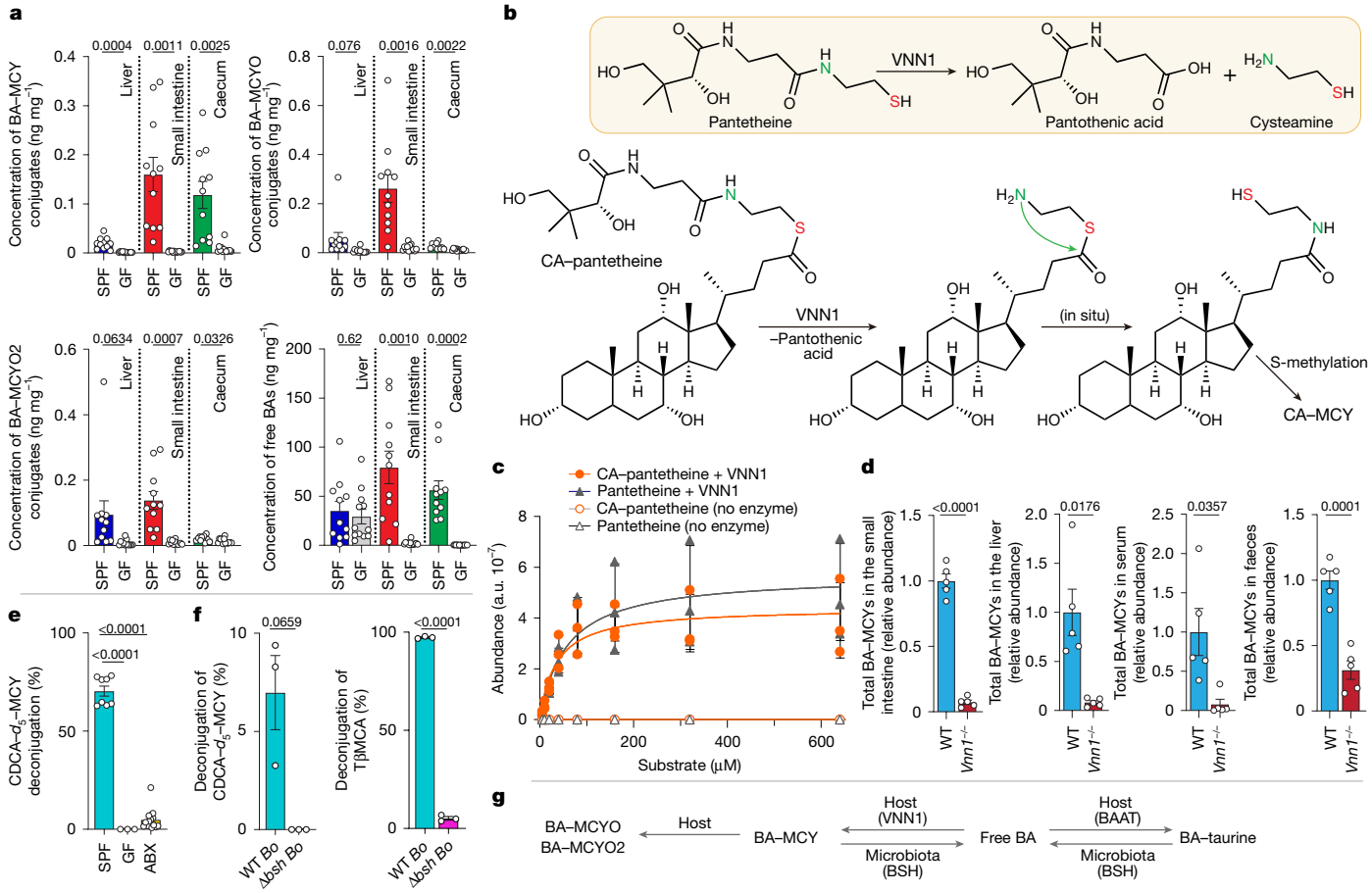

Fig. 3 | Host-dependent production of BA–MCYs and microbial deconjugation. **a**, Total amounts of BA–MCY conjugates and corresponding free BAs in the liver, small intestine and caecum of SPF ($n = 11$) and germ-free ($n = 12$ for the liver and $n = 13$ for the small intestine and caecum) mice. **b**, Established function of VNN1 in pantetheine hydrolysis (box; top) and the proposed role of VNN1 in CA–pantetheine hydrolysis, followed by rearrangement and methylation to form CA–MCY (bottom). **c**, Production of pantothenic acid from a range of concentrations of CA–pant and pantetheine incubated with recombinant VNN1 in vitro. The reactions with both substrates follow saturation kinetics. The enzyme concentration was 0.01 μM. The reactions were incubated at 37 °C for 15 min. The number of independent assays using the same batch of enzyme was three. **d**, Relative abundances of BA–MCY conjugates in the small intestine, liver, serum and faeces of WT ($n = 5$) or *Vnn1*$^{-/-}$ ($n = 5$) mice. **e**, Deconjugation of supplemented CDCA–d_5–MCY in the faeces of SPF ($n = 8$), germ-free ($n = 3$) and ABX ($n = 15$) mice. **f**, Deconjugation of MCY or taurine conjugates of BA in the faeces of germ-free monocolonized with WT ($n = 3$) or BSH-deleted *B. ovatus* ($n = 3$; WT *Bo* or *Δbsh Bo*, respectively). Data are shown as mean ± s.e.m. (**a**,**d**–**f**) or mean ± s.d. (**c**), and *P* values were calculated using unpaired two-sided Student's *t*-test with Welch's correction. **g**, Roles of host and microbiota in the biosynthesis and metabolism of BA–taurine and BA–MCY conjugates.

analysis revealed incorporation of deuterium in both the BA–taurine and the BA–MCY conjugates (Extended Data Fig. 4b,c), consistent with a cysteine origin of both taurine and the MCY moiety. As expected, we also observed deuterium incorporation into the CoA breakdown product pantetheine (Extended Data Fig. 4d).

These results support a model in which the BA–MCY conjugates are derived from acylation of a cysteamine derivative other than taurine. Next, we considered whether the conjugation is likely to be mediated by the microbiota or the host. Although the abundances of the BA–MCY conjugates were strongly microbiota dependent, their production was not abolished in germ-free animals (Fig. 2a,b and Extended Data Fig. 2a–d), suggesting that the conjugation reaction itself does not require the microbiota. Therefore, we next investigated whether BA–MCY production is related to the biosynthesis of BA–taurine conjugates. Conjugation of BAs with taurine and amino acids in the liver is mediated by BAAT, a type 1 acyl-CoA thioesterase (ACOT). Members of this gene family catalyse a wide range of acyl transfer reactions[35]; putative conjugates of BAs with cysteamine and methylcysteamine have recently been reported to accumulate in *Baat*$^{-/-}$ mice[36]. We confirmed that the BA cysteamine derivatives accumulating in *Baat*$^{-/-}$ mice are identical with the compounds that we identified (Extended Data Fig. 5a–d), demonstrating that BA–MCY biosynthesis is distinct from BA–taurine conjugation. Lack of taurine conjugation in *Baat*$^{-/-}$ mice results in greatly increased levels of both free BAs and BA–MCY conjugates[36] (Extended Data Fig. 5e,f), consistent with parallel increase of free BAs and BA–MCY conjugates observed in mice fed a high-fibre diet. Suppression of microbiota in *Baat*$^{-/-}$ mice does not diminish the elevated levels of BA–MCY in this mutant strain[36]. Together, our results indicate that BA–MCYs are derived from a host-dependent conjugation pathway that exists in parallel with conjugation of BAs with taurine.

Next, we considered potential sites of BA–MCY biosynthesis. Although BA–taurine conjugates are produced in the liver, the fact that BA–MCY levels are governed primarily by the abundance of free BAs, which in SPF mice are predominantly derived from deconjugation of BA–taurine and BA–glycine by the intestinal microbiota, suggested that the intestine may be involved in BA–MCY production. Therefore, we additionally profiled BA–MCY levels in the small intestine and caecum, which revealed that BA–MCY conjugates are much more abundant in intestinal tissues than in the liver (Fig. 3a and Extended Data Fig. 6). Moreover, the ratio of BA–MCY conjugates relative to their oxidation products BA–MCYO and BA–MCYO2 was higher in intestinal tissues than in the liver, serum and faeces (Fig. 3a and Supplementary

Table 3), suggesting that BA–MCY conjugates are produced from free BAs following their reuptake in the intestine. A model in which intestinal production of BA–MCYs is dependent on reuptake of free BAs was further consistent with our observation that, across different diets and conditions, abundances of free BAs and BA–MCYs are correlated (Extended Data Fig. 3a–c).

BA–MCY biosynthesis depends on host VNN1

As BA–MCY conjugates could plausibly be derived from pantetheine breakdown, we sought to test whether BA–MCY biosynthesis may proceed via the pantetheinase VNN1, which is highly expressed in intestinal tissues[37,38], where BA–MCY concentrations were highest. The primary function of VNN1 is to hydrolyse pantetheine into cysteamine and pantothenic acid (Fig. 3b), as part of CoA recycling, and recent studies have shown that VNN1 has important roles in the regulation of metabolism, inflammation and associated diseases[37,39]. Although VNN1 could be a plausible source for the cysteamine moiety required for BA–MCY production, we hypothesized that, in addition to hydrolysing pantetheine, VNN1 may also be capable of hydrolysing BA–pantetheine or BA–CoA conjugates. The resulting S-linked BA–cysteamine derivatives would then rearrange to the N-linked isomer, which following S-methylation would produce the BA–MCY conjugates (Fig. 3b). To investigate this hypothesis, we first tested whether recombinant VNN1 could hydrolyse a synthetic cholic acid–pantetheine conjugate (CA–pant). We found that VNN1 breaks down CA–pant as efficiently as pantetheine (Fig. 3c and Extended Data Fig. 7a) and further showed that the resulting CA–cysteamine conjugate rearranges to the corresponding cholic acid–cysteamide (CA–CY), a plausible precursor of CA–MCY that we had also detected in *Baat*$^{-/-}$ mice (Extended Data Fig. 7b). To assess whether VNN1 contributes to BA–MCY biosynthesis in vivo, we compared BA profiles of wild-type (WT) and *Vnn1*$^{-/-}$ mice in various tissues (Fig. 3d). We found that BA–MCY levels are dramatically reduced in the small intestine, liver and serum, and, to a lesser extent, in the faeces of *Vnn1*$^{-/-}$-mutant mice (Fig. 3d). These results indicate that in vivo BA–MCY biosynthesis largely depends on the host enzyme VNN1. Furthermore, we found that the predicted precursor of CA–CY, CA–pant, accumulates in the small intestine and faeces of *Vnn1*$^{-/-}$ mice, whereas this compound was absent in the corresponding WT samples and also could not be detected in the *Vnn1*$^{-/-}$ liver and serum, suggesting that BA–pantetheine conjugates are direct precursors for BA–MCY biosynthesis in the intestine (Extended Data Fig. 7c,d).

Microbial and host metabolism of BA–MCYs

Taurine and glycine BA conjugates are efficiently deconjugated in the gut by microbial bile salt hydrolases (BSHs)[3,4,32,40], generating free BAs. Correspondingly, the ratio of BA–taurine conjugates to free BAs was dramatically increased in faeces of germ-free compared with SPF mice (Extended Data Fig. 8a,b). Considering the possibility that the gut microbiota may also have a role in the deconjugation of BA–MCYs, we noted that, even though BA–MCY levels are reduced in germ-free mice (Extended Data Figs. 2b–d and 8c), the ratio of BA–MCY conjugates to free BAs was greatly increased in germ-free compared with SPF faecal samples (Extended Data Fig. 8a). In fact, BA–MCY levels were similar to or exceeded levels of free BAs in faeces of germ-free mice (Extended Data Fig. 8d).

To determine whether BA–MCYs can indeed be deconjugated by the microbiota, we analysed faecal and liver samples from SPF and germ-free mice supplemented with stable-isotope-labelled CDCA–d_5–MCY for the presence of free labelled CDCA and other labelled BAs that can be derived from CDCA. To broadly survey metabolism of BA–MCYs, we additionally compared supplemented and control mice via untargeted metabolomics using the Label Finder approach in the Metaboseek platform[31]. Targeted analysis of faecal samples from CDCA–d_5–MCY-supplemented SPF mice revealed CDCA–d_5–MCY as well as d_4-labelled and d_5-labelled free CDCA (Extended Data Fig. 8e–g and Supplementary Fig. 5a,b), indicating that BA–MCYs can be deconjugated in the gut. In addition, we detected labelled versions of other free BAs that can be derived from CDCA (Extended Data Fig. 8f and Supplementary Fig. 5b), whereas CA, DCA and other CA-derived BAs remained unlabelled (Supplementary Fig. 5b), consistent with their separate biosynthetic pathway[23,41]. Analysis of faecal and liver samples from CDCA–d_5–MCY-supplemented SPF mice further indicated that labelled free BAs derived from supplemented CDCA–d_5–MCY are partly reconjugated with taurine (Extended Data Fig. 8h–m and Supplementary Table 4). Label Finder analysis additionally revealed that the remainder of supplemented CDCA–d_5–MCY that was not deconjugated was converted into its oxidized derivative, CDCA–$d_{4/5}$–MCYO and, to a lesser extent, CDCA–$d_{4/5}$–MCYO2. In fact, only trace amounts of CDCA–d_5–MCY could be detected in the liver of supplemented mice, indicating that supplemented CDCA–d_5–MCY is quickly oxidized to CDCA–$d_{4/5}$–MCYO(2) (Extended Data Fig. 8k,m).

In contrast to SPF mice, deconjugation-derived, labelled CDCA or other labelled free BAs were not detected in germ-free mice supplemented with CDCA–d_5–MCY (Fig. 3e and Supplementary Fig. 5c,d), indicating that deconjugation of CDCA–MCY is dependent on microbiota. Similarly, suppression of microbiota in SPF mice treated with antibiotics (ABX) resulted in significantly reduced deconjugation of supplemented CDCA–d_5–MCY compared with SPF mice (Fig. 3e and Extended Data Fig. 8f,g,j,k). In ABX and germ-free mice, supplemented CDCA–d_5–MCY was instead primarily converted into the corresponding oxidation products, CDCA–$d_{4/5}$–MCYO and CDCA–$d_{4/5}$–MCYO2 (Extended Data Fig. 8g,k,m and Supplementary Table 4).

Next, we demonstrated that BA–MCY conjugates are deconjugated by faecal suspensions obtained from SPF mice and individual gut bacteria known to have the gene encoding BSH[42] (Extended Data Fig. 9a,b). To determine whether BSH is required for BA–MCY deconjugation, we tested gnotobiotic mice colonized with *Bacteroides ovatus* ATCC 8483 (WT *Bo*) or a *B. ovatus*-mutant strain in which we deleted the BSH-encoding gene BO_02350 (*Δbsh Bo*)[32,40]. We found that CDCA–d_5–MCY was partially deconjugated in the gnotobiotic mice colonized with WT *Bo*, but was not deconjugated in mice colonized with mutant *Δbsh Bo* (Fig. 3f), where the supplemented CDCA–d_5–MCY was exclusively converted to the oxidized CDCA–$d_{4/5}$–MCYO(2), as in germ-free mice (Extended Data Fig. 9c). These results indicate that BSH of gut microbiota can deconjugate BA–MCY conjugates, albeit less efficiently than the corresponding taurine conjugates (Fig. 3f), and that, in the absence of microbiota, BA–MCY conjugates are metabolized by the host into the corresponding BA–MCYO and BA–MCYO2 derivatives (Fig. 3g).

BA–MCYs act as FXR antagonists in vitro

For functional evaluation of the BA–MCY conjugates, we focused on FXR, one of the major endogenous targets of BAs in vertebrates. Free BAs, for example, the broadly conserved CDCA, CA and DCA[14], as well amino acid conjugates of CA[43], function as potent FXR agonists that negatively regulate BA production. By contrast, it is unclear whether there are any conserved endogenous FXR antagonists that would promote BA production.

To test for potential FXR agonist or antagonist activity of the identified BA–MCY conjugates, we selected four derivatives, CA–MCY, CA–MCYO, βMCA–MCY and CDCA–MCY based on their relative abundance in SPF mouse serum samples and considering previously reported FXR agonist activity of the corresponding free BAs[14]. We assayed these four compounds in agonist and antagonist modes using a protein–protein interaction assay between the full-length human FXR protein and a steroid receptor co-activator peptide (SRCP)-derived nuclear fusion protein[44]. Whereas none of the tested conjugates showed agonist activity at any of the tested concentrations (Fig. 4 and Extended Data

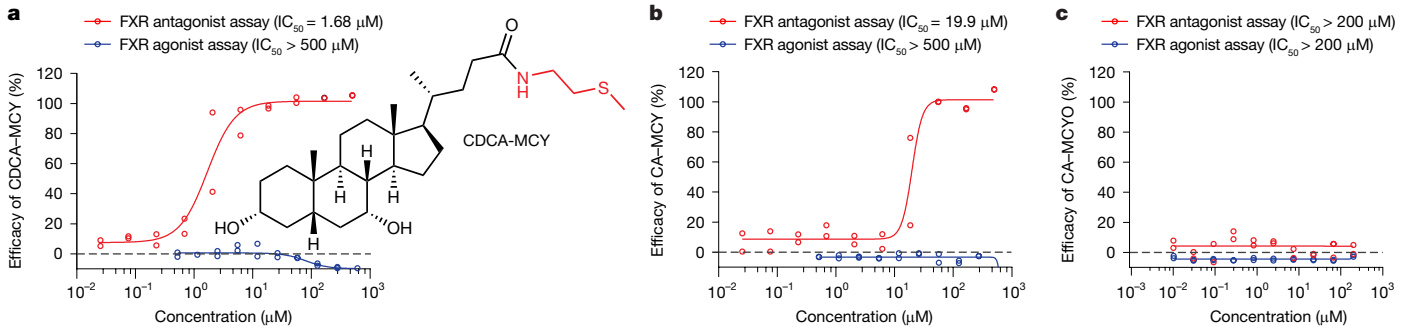

Fig. 4 | BA–MCY conjugates are FXR antagonists. a–c, BA–MCYs act as FXR antagonists in vitro. Compounds were tested against a cell-based protein–protein interaction assays in both agonist and antagonist modes. CDCA–MCY (**a**) and CA–MCY (**b**) showed strong FXR antagonistic effects to GW4604-mediated activation of FXR, whereas CA–MCYO (**c**) showed no FXR antagonistic effects. None of the tested BA–MCY conjugates showed FXR agonistic effects in this assay (also see Extended Data Fig. 10). Assays were performed in duplicate for each concentration.

Fig. 10a,b), CDCA–MCY, CA–MCY and βMCA–MCY showed potent antagonistic activity with IC_{50} values of 1.68, 19.9 and 104.5 μM, respectively, against GW4604-mediated activation of FXR[45] (Fig. 4a,b and Extended Data Fig. 10a). By contrast, CA–MCYO was inactive, indicating that sulfur oxidation abolished antagonistic activity (Fig. 4c). CDCA–MCY also inhibited FXR activation mediated by CDCA and the more potent synthetic BA obeticholic acid (Extended Data Fig. 10c–g). In parallel, we also tested TβMCA, which had previously been reported as a weak, mouse-specific FXR antagonist[24]. However, TβMCA was inactive at the tested range of concentrations in this assay (Extended Data Fig. 10h). These results suggest that BA–MCY conjugates function as endogenous FXR antagonists that complement the role of free BAs as FXR agonists.

BA–MCYs regulate FXR signalling in vivo

BA biosynthesis in the liver is controlled by a complex signalling network regulated by hepatic and intestinal FXR via distinct pathways[23,28,41] (Fig. 5a). In the liver, FXR agonists promote expression of short heterodimer partner (SHP), which in turn antagonizes expression of *Cyp7a1*, encoding a cytochrome P450 enzyme required for the first and rate-limiting step in BA synthesis[23,28,41] (Fig. 5a). In addition, SHP expression suppresses *Cyp8b1*, which catalyses the conversion of the BA precursor 7α-hydroxy-4-cholesten-3-one into 7α,12α-dihydroxy-4-cholesten-3-one and thereby controls the balance between the relative amounts of BAs that are 12α-hydroxylated (such as CA) and BAs that are not 12α-hydroxylated (such as CDCA). In contrast, intestinal FXR activation promotes production of the ileal hormone fibroblast growth factor 15 (FGF15; FGF19 in humans), a signalling peptide that travels to the liver via the enterohepatic circulation to suppress expression of *Cyp7a1*. Conversely, FXR antagonists promote BA synthesis by relieving repression of *Cyp7a1* and *Cyp8b1* by suppressing SHP and FGF15/FGF19 expression[24,39–41] (Fig. 5a).

To determine whether BA–MCYs affect FXR-dependent regulation of BA biosynthesis in vivo, we supplemented SPF mice via oral gavage with CDCA–MCY, which had shown the highest potency in our in vitro FXR antagonist assay (Fig. 4a). Gene expression analysis indicated that *Cyp7a1* and *Cyp8b1* expression in the liver was significantly increased (Fig. 5b). In addition, we found that ileal *Shp* mRNA and serum FGF15 levels were significantly decreased in mice supplemented with CDCA–MCY (Fig. 5c,d), suggesting that increased expression of *Cyp7a1* is in part due to antagonism of the intestinal FXR–FGF15 pathway. Increased *Cyp8b1* expression, which is largely independent of the intestinal FXR–FGF15 pathway[46–48], suggests that liver FXR may also be affected by CDCA–MCY supplementation, or that other pathways contribute to FXR-dependent ileum-to-liver signalling[49]. Because we found that BA–MCY production may be dependent on reabsorption of free BAs from the ileum, we additionally tested whether CDCA–MCY supplementation affects expression of *Slc10a2*, the transporter mediating BA reuptake from the gut; however, *Slc10a2* expression was unchanged (Fig. 5e).

To measure the effects of CDCA–MCY on BA production in vivo, we conducted additional supplementation studies using stable isotope-labelled CDCA–d_5–MCY. The use of labelled CDCA–d_5–MCY avoided potentially confounding effects arising from deconjugation and further metabolism of the supplemented CDCA–MCY, as it allowed us to distinguish unambiguously between BAs derived from the supplemented, labelled CDCA–d_5–MCY and de novo-produced, unlabelled BAs (Extended Data Fig. 8e). Quantification of BA levels from CDCA–d_5–MCY-supplemented animals showed a strong increase of unlabelled CDCA-derived BAs in faecal samples (Fig. 5f and Extended Data Fig. 11a). Similarly, levels of CA-derived BAs were increased in faecal samples of animals supplemented with CDCA–d_5–MCY or CDCA–MCY (Fig. 5g and Extended Data Fig. 11b). Faecal BA levels were also increased by CDCA–d_5–MCY supplementation in ABX mice (Extended Data Fig. 11c). Given that levels of unlabelled BAs in the liver and serum of supplemented mice were not significantly changed (Extended Data Fig. 11d–g), the large increase in faecal excretion of both CA-family and CDCA-family BAs indicates strong upregulation of BA production in CDCA–MCY-supplemented animals, in line with the increased expression of BA biosynthesis genes[47,48,50,51] (Fig. 5b).

Next, we tested whether upregulation of BA synthesis by CDCA–MCY supplementation is in fact dependent on FXR. We found that CDCA–MCY supplementation increased faecal BA abundance in WT mice but not in FXR-deficient (*Nr1h4*$^{-/-}$) mice (Fig. 5h). BA levels in the liver and serum of WT and *Nr1h4*$^{-/-}$ mice were not significantly affected by CDCA supplementation (Extended Data Fig. 12a,b), consistent with results from our initial supplementation study (Extended Data Fig. 11d–g). These data demonstrate that CDCA–MCY supplementation increases BA biosynthesis in an FXR-dependent manner.

Given that intestinal FXR antagonists have been shown to alleviate hepatic steatosis in mouse models of obesity[46,52], we asked whether CDCA–MCY supplementation could improve lipid accumulation in the liver of mice fed a high-cholesterol diet (HCD). Liver histology and oil red O staining revealed greatly decreased hepatic lipid accumulation in CDCA–MCY-supplemented HCD-fed mice compared with untreated HCD-fed mice (Fig. 5i,j), consistent with previous studies of synthetic compounds acting as intestinal FXR antagonists[46,52]. We observed similar effects when CDCA–MCY was supplied at a tenfold lower dose (Extended Data Fig. 12c,d).

Together, our results support a model in which host-derived BA–MCY conjugates act as intestinal FXR antagonists that balance the FXR agonistic activity of microbiota-derived free BAs, as part of a regulatory circuitry that fine tunes BA signalling within the hepatobiliary system (Fig. 5k).

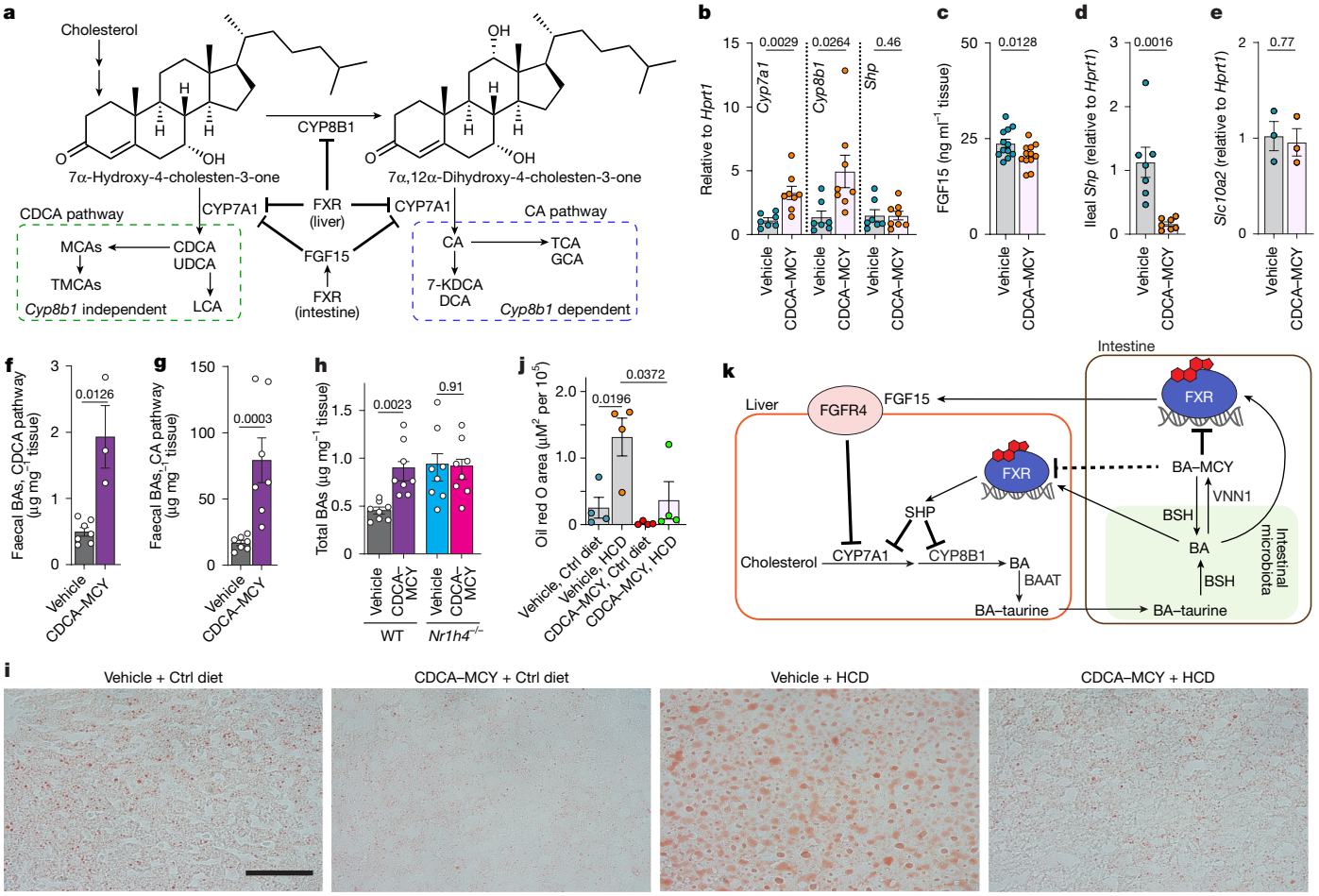

Fig. 5 | BA–MCYs regulate BA biosynthesis in vivo and a model for the role of BA–MCYs in BA metabolism. a, BA biosynthesis scheme, highlighting separate CA and CDCA pathways. The compounds highlighted in blue and green (dashed outlines) belong to the CA and CDCA pathways, respectively. **b**, Gene expression ratio of *Shp*, *Cyp8b1* and *Cyp7a1* to *Hprt1* control in the liver of mice administered CDCA–MCY ($n = 4$) or control (corn oil; $n = 3$). **c**, Serum FGF15 levels of mice administered CDCA–d_5–MCY or control ($n = 12$). **d**, Gene expression ratio of *Shp* to *Hprt1* control in the small intestine of mice administered CDCA–d_5–MCY or control ($n = 7$). **e**, Gene expression ratio of *Slc10a2* to *Hprt1* control in the small intestine of mice administered CDCA–d_5–MCY or control ($n = 3$). **f**,**g**, Abundances of endogenously produced BAs in the faeces of mice administered CDCA–MCY or CDCA–d_5–MCY for 14 days. The total amounts of CDCA-derived BAs (**f**; $n = 7$ for control and $n = 3$ for CDCA–d_5–MCY-fed mice) and CA-derived BAs (**g**; $n = 7$ for control and $n = 7$ for CDCA–MCY ($n = 4$) or CDCA–d_5–MCY ($n = 3$) fed mice) are shown. **h**, Abundances of endogenously produced BAs in the faeces of WT or *Nr1h4*$^{-/-}$ mice administered CDCA–d_5–MCY daily for 14 days. The total amounts of BAs ($n = 8$ for control and $n = 8$ for CDCA–MCY-fed mice) are shown. **i**, Representative photomicrographs of oil red O staining of liver sections of mice treated with the indicated conditions. Mice were fed control (Ctrl; $n = 4$ for vehicle and $n = 4$ for CDCA–MCY) or a HCD ($n = 4$ for vehicle and $n = 4$ for CDCA–MCY). CDCA–MCY was delivered by oral gavage at a rate of 50 mg kg^{-1} body weight daily for 2 weeks. Scale bar, 50 μm. **j**, Average measured oil red O area in panel **i**. **k**, Proposed model for FXR-dependent regulation of BA metabolism by BA–MCYs. Panel **k** was adapted from ref. 60, Elsevier. Data are shown as mean ± s.e.m. (**b**–**h**,**j**). *P* values were calculated using unpaired two-sided Student's *t*-test with Welch's correction (**b**–**h**) or one-way analysis of variance with Tukey's correction (**j**).

Discussion

BAs represent gut microbiota-dependent metabolites whose pervasive effects on human physiology are among the most well studied[4,7,43,53,54]. Correspondingly, the biochemical mechanisms by which the host may regulate their activities are of substantial interest in the context of human health and disease. In the case of BAs, their taurine conjugation by the host and subsequent deconjugation by intestinal microbiota provide a classical example for the regulation of metabolite abundance via opposing host-dependent and microbiota-dependent pathways. Our identification of VNN1-dependent BA–MCY conjugates as FXR antagonists reveals a previously unrecognized host-dependent layer of BA metabolism that counteracts the physiological functions of free BAs (Fig. 5k). In vitro protein–protein interaction assays demonstrated strong FXR antagonistic activity for CA–MCY, CDCA–MCY and βMCA–MCY (Fig. 4a,b and Extended Data Fig. 10a), whereas free BAs generally act as FXR agonists[14]. Supplementation of mice with CDCA–MCY increased total BA production and expression of the enzymes that catalyse the rate-limiting steps in BA biosynthesis, consistent with CDCA–MCY functioning as an FXR antagonist in vivo. This is in contrast to its parent compound CDCA, which acts as an FXR agonist and reduces overall BA levels[55]. BA–MCYs were most abundant in intestinal tissues (Fig. 3a), where VNN1 is highly expressed, and appeared to get oxidized quickly into the inactive BA–MCYO derivatives when entering the general circulation. Similar to other intestinal FXR antagonists[46,52], CDCA–MCY supplementation alleviated hepatic lipid accumulation in mice fed a HCD (Fig. 5i,j). Thus, it seems likely that, following their reuptake in the intestine, conversion of free BAs (FXR agonists) into BA–MCYs (FXR antagonists) via the pantetheinase VNN1 represents an important component of the feedback mechanisms regulating BA biosynthesis and other FXR-dependent phenotypes, including diverse aspects of fatty acid metabolism[15,56,57]. Given the dysregulation of BA

levels in type II diabetes, metabolic syndrome and the cholestatic diseases[12,58,59], BA–MCYs may have substantial therapeutic potential. We further demonstrate that dietary fibre can upregulate production of BA–MCY conjugates in mice, suggesting that the levels of these conjugates can be regulated by diet and prebiotic or probiotic supplements, which may have translational potential in conditions of dysregulated immune or metabolic homeostasis.

The profound effects of MCY conjugation on the biological activity of BAs led us to investigate the roles of both host and microbiota in the production of the MCY conjugates. Levels of unconjugated, free BAs are largely dependent on microbiota, as the vast majority of free BAs in SPF mice is derived from microbial deconjugation of the corresponding taurine conjugates. Using a series of stable isotope supplementation studies, we have shown that BA–MCYs are derived from conjugation with cysteamine or another CoA-derived metabolite, instead of reduction of corresponding taurine derivatives. Consistent with the idea that BA–taurine and BA–MCY conjugates have distinct biosynthetic origins, BA–MCY conjugates accumulate in mice deficient in the enzyme conjugating BAs with taurine (BAAT)[36]. The intriguing connection to CoA breakdown metabolism led us to uncover the role of the pantetheinase VNN1 for BA–MCY production, demonstrating that a host enzyme that is highly expressed in the intestine, the site of BA reuptake, has a central role for BA–MCY production (Fig. 3d and Extended Data Fig. 7d). BA–MCY biosynthesis is strongly reduced but not fully abolished in *Vnn1*$^{-/-}$ mice, suggesting that other pantetheinases (VNN3 in mouse or VNN2 in humans) may also contribute. Furthermore, although bacteria have no close homologues of vertebrate pantetheinases, it is possible that other bacterial hydrolases or peptidases have similar activity and also contribute to the residual amounts of BA–MCYs observed in *Vnn1*$^{-/-}$ mice.

VNN1 serves diverse functions in lipid metabolism and forms an important link between lipid accumulation and hepatic diseases[37,39], which is of particular interest in light of our finding that BA–MCY supplementation alleviated lipid accumulation in the liver of HCD mice (Fig. 5i,j). Clarifying the role of VNN1 for BA–MCY production and other aspects of BA metabolism in the intestine and other tissues may provide new insights in associated phenotypes. More generally, the identification of the role of VNN1 in BA–MCY production reveals an intriguing connection between BA signalling and CoA breakdown pathways, which are extensively regulated by nutritional state, feeding back on many other aspects of metabolism[34]. BA–MCY conjugates can be hydrolysed by microbial BSH, albeit perhaps less efficiently than BA–taurine conjugates. To what extent microbial deconjugation of BA–MCYs is physiologically relevant is unclear; however, it may represent an additional mechanism by which the microbiota contribute to regulating the balance of FXR agonists and antagonists.

Together, our results suggest that MCY conjugation of BAs by the host balances microbiota-dependent taurine deconjugation, as part of a metabolic network integrating host-derived and microbiota-derived pathways that regulates FXR-dependent BA production, fat metabolism, CoA metabolism and possibly other processes downstream of BAs.

Online content

Any methods, additional references, Nature Portfolio reporting summaries, source data, extended data, supplementary information, acknowledgements, peer review information; details of author contributions and competing interests; and statements of data and code availability are available at https://doi.org/10.1038/s41586-024-08379-9.

1. Robertson, R. C., Manges, A. R., Finlay, B. B. & Prendergast, A. J. The human microbiome and child growth — first 1000 days and beyond. *Trends Microbiol.* **27**, 131–147 (2019).
2. Fuchs, C. D. & Trauner, M. Role of bile acids and their receptors in gastrointestinal and hepatic pathophysiology. *Nat. Rev. Gastroenterol. Hepatol.* **19**, 432–450 (2022).
3. Thomas, C., Pellicciari, R., Pruzanski, M., Auwerx, J. & Schoonjans, K. Targeting bile-acid signalling for metabolic diseases. *Nat. Rev. Drug Discov.* **7**, 678–693 (2008).
4. Wahlstrom, A., Sayin, S. I., Marschall, H. U. & Backhed, F. Intestinal crosstalk between bile acids and microbiota and its impact on host metabolism. *Cell Metab.* **24**, 41–50 (2016).
5. Belkaid, Y. & Hand, T. W. Role of the microbiota in immunity and inflammation. *Cell* **157**, 121–141 (2014).
6. Blander, J. M., Longman, R. S., Iliev, I. D., Sonnenberg, G. F. & Artis, D. Regulation of inflammation by microbiota interactions with the host. *Nat. Immunol.* **18**, 851–860 (2017).
7. Hang, S. Y. et al. Bile acid metabolites control T_H17 and T_{reg} cell differentiation. *Nature* **576**, 143–148 (2019).
8. Morais, L. H., Schreiber, H. L. T. & Mazmanian, S. K. The gut microbiota–brain axis in behaviour and brain disorders. *Nat. Rev. Microbiol.* https://doi.org/10.1038/s41579-020-00460-0 (2020).
9. Fan, Y. & Pedersen, O. Gut microbiota in human metabolic health and disease. *Nat. Rev. Microbiol.* **19**, 55–71 (2021).
10. Nicholson, J. K. et al. Host–gut microbiota metabolic interactions. *Science* **336**, 1262–1267 (2012).
11. Martin, A. M., Sun, E. W., Rogers, G. B. & Keating, D. J. The influence of the gut microbiome on host metabolism through the regulation of gut hormone release. *Front. Physiol.* **10**, 428 (2019).
12. Molinaro, A., Wahlstrom, A. & Marschall, H. U. Role of bile acids in metabolic control. *Trends Endocrinol. Metab.* **29**, 31–41 (2018).
13. Ramírez-Pérez, O., Cruz-Ramón, V., Chinchilla-López, P. & Méndez-Sánchez, N. The role of the gut microbiota in bile acid metabolism. *Ann. Hepatol.* **16**, s15–s20 (2017).
14. Wang, H., Chen, J., Hollister, K., Sowers, L. C. & Forman, B. M. Endogenous bile acids are ligands for the nuclear receptor FXR/BAR. *Mol. Cell* **3**, 543–553 (1999).
15. Claudel, T., Staels, B. & Kuipers, F. The farnesoid X receptor — a molecular link between bile acid and lipid and glucose metabolism. *Arterioscler. Thromb. Vasc. Biol.* **25**, 2020–2031 (2005).
16. Jiang, L., Zhang, H., Xiao, D., Wei, H. & Chen, Y. Farnesoid X receptor (FXR): structures and ligands. *Comput. Struct. Biotechnol. J.* **19**, 2148–2159 (2021).
17. Johnson, M. R., Barnes, S., Kwakye, J. B. & Diasio, R. B. Purification and characterization of bile acid-CoA:amino acid *N*-acyltransferase from human liver. *J. Biol. Chem.* **266**, 10227–10233 (1991).
18. Killenberg, P. G. & Jordan, J. T. Purification and characterization of bile acid-CoA:amino acid *N*-acyltransferase from rat liver. *J. Biol. Chem.* **253**, 1005–1010 (1978).
19. Funabashi, M. et al. A metabolic pathway for bile acid dehydroxylation by the gut microbiome. *Nature* **582**, 566–570 (2020).
20. White, B. A., Lipsky, R. L., Fricke, R. J. & Hylemon, P. B. Bile acid induction specificity of 7α-dehydroxylase activity in an intestinal Eubacterium species. *Steroids* **35**, 103–109 (1980).
21. Jones, B. V., Begley, M., Hill, C., Gahan, C. G. & Marchesi, J. R. Functional and comparative metagenomic analysis of bile salt hydrolase activity in the human gut microbiome. *Proc. Natl Acad. Sci. USA* **105**, 13580–13585 (2008).
22. Ridlon, J. M., Harris, S. C., Bhowmik, S., Kang, D. J. & Hylemon, P. B. Consequences of bile salt biotransformations by intestinal bacteria. *Gut Microbes* **7**, 22–39 (2016).
23. Pandak, W. M. & Kakiyama, G. The acidic pathway of bile acid synthesis: not just an alternative pathway. *Liver Res.* **3**, 88–98 (2019).
24. Sayin, S. I. et al. Gut microbiota regulates bile acid metabolism by reducing the levels of tauro-β-muricholic acid, a naturally occurring FXR antagonist. *Cell Metab.* **17**, 225–235 (2013).
25. Sun, L. et al. Gut microbiota and intestinal FXR mediate the clinical benefits of metformin. *Nat. Med.* **24**, 1919–1929 (2018).
26. Makishima, M. et al. Identification of a nuclear receptor for bile acids. *Science* **284**, 1362–1365 (1999).
27. Reschly, E. J. et al. Evolution of the bile salt nuclear receptor FXR in vertebrates. *J. Lipid Res.* **49**, 1577–1587 (2008).
28. Chiang, J. Y. Bile acids: regulation of synthesis. *J. Lipid Res.* **50**, 1955–1966 (2009).
29. Brandman, O. & Meyer, T. Feedback loops shape cellular signals in space and time. *Science* **322**, 390–395 (2008).
30. Tautenhahn, R., Patti, G. J., Rinehart, D. & Siuzdak, G. XCMS Online: a web-based platform to process untargeted metabolomic data. *Anal. Chem.* **84**, 5035–5039 (2012).
31. Helf, M. J., Fox, B. W., Artyukhin, A. B., Zhang, Y. K. & Schroeder, F. C. Comparative metabolomics with Metaboseek reveals functions of a conserved fat metabolism pathway in *C. elegans*. *Nat. Commun.* **13**, 782 (2022).
32. Arifuzzaman, M. et al. Inulin fibre promotes microbiota-derived bile acids and type 2 inflammation. *Nature* https://doi.org/10.1038/s41586-022-05380-y (2022).
33. Singh, V. et al. Dysregulated microbial fermentation of soluble fiber induces cholestatic liver cancer. *Cell* **175**, 679–694.e22 (2018).
34. Naquet, P., Kerr, E. W., Vickers, S. D. & Leonardi, R. Regulation of coenzyme A levels by degradation: the 'ins and outs'. *Prog. Lipid Res.* **78**, 101028 (2020).
35. Hunt, M. C., Siponen, M. I. & Alexson, S. E. The emerging role of acyl-CoA thioesterases and acyltransferases in regulating peroxisomal lipid metabolism. *Biochim. Biophys. Acta* **1822**, 1397–1410 (2012).
36. Neugebauer, K. A. et al. BAAT gene knockout alters early life development and the gut microbiome and reveals unusual bile acids in mice. *J. Lipid Res.* **63**, 100297 (2022).
37. Bartucci, R., Salvati, A., Olinga, P. & Boersma, Y. L. Vanin 1: its physiological function and role in diseases. *Int. J. Mol. Sci.* **20**, 3891 (2019).
38. Kaskow, B. J., Proffitt, J. M., Blangero, J., Moses, E. K. & Abraham, L. J. Diverse biological activities of the vascular non-inflammatory molecules — the vanin pantetheinases. *Biochem. Biophys. Res. Commun.* **417**, 653–658 (2012).
39. Yu, H. et al. Vanin1 (VNN1) in chronic diseases: future directions for targeted therapy. *Eur. J. Pharmacol.* **962**, 176220 (2024).
40. Yao, L. et al. A selective gut bacterial bile salt hydrolase alters host metabolism. *eLife* https://doi.org/10.7554/eLife.37182 (2018).
41. Al-Dury, S., Wahlstrom, A., Stahlman, M., Backhed, F. & Marschall, H. U. Cyp3a11 is dispensable for the formation of murine bile acids. *J. Hepatol.* **64**, S436 (2016).
42. Guzior, D. V. et al. Bile salt hydrolase acyltransferase activity expands bile acid diversity. *Nature* https://doi.org/10.1038/s41586-024-07017-8 (2024).

43. Quinn, R. A. et al. Global chemical effects of the microbiome include new bile-acid conjugations. *Nature* **579**, 123–129 (2020).
44. Voegel, J. J., Heine, M. J., Zechel, C., Chambon, P. & Gronemeyer, H. TIF2, a 160 kDa transcriptional mediator for the ligand-dependent activation function AF-2 of nuclear receptors. *EMBO J.* **15**, 3667–3675 (1996).
45. Willson, T. M., Jones, S. A., Moore, J. T. & Kliewer, S. A. Chemical genomics: functional analysis of orphan nuclear receptors in the regulation of bile acid metabolism. *Med. Res. Rev.* **21**, 513–522 (2001).
46. Jiang, C. et al. Intestine-selective farnesoid X receptor inhibition improves obesity-related metabolic dysfunction. *Nat. Commun.* **6**, 10166 (2015).
47. Inagaki, T. et al. Fibroblast growth factor 15 functions as an enterohepatic signal to regulate bile acid homeostasis. *Cell Metab.* **2**, 217–225 (2005).
48. Kim, I. et al. Differential regulation of bile acid homeostasis by the farnesoid X receptor in liver and intestine. *J. Lipid Res.* **48**, 2664–2672 (2007).
49. Gonzalez, F. J., Jiang, C., Xie, C. & Patterson, A. D. Intestinal farnesoid X receptor signaling modulates metabolic disease. *Dig. Dis.* **35**, 178–184 (2017).
50. Cheng, K. et al. Diminished gallbladder filling, increased fecal bile acids, and promotion of colon epithelial cell proliferation and neoplasia in fibroblast growth factor 15-deficient mice. *Oncotarget* **9**, 25572–25585 (2018).
51. Ito, S. et al. Impaired negative feedback suppression of bile acid synthesis in mice lacking betaKlotho. *J. Clin. Invest.* **115**, 2202–2208 (2005).
52. Kuang, J. L. et al. Hyodeoxycholic acid alleviates non-alcoholic fatty liver disease through modulating the gut–liver axis. *Cell Metab.* **35**, 1752–1766.e8 (2023).
53. Song, X. Y. et al. Microbial bile acid metabolites modulate gut RORγ$^+$ regulatory T cell homeostasis. *Nature* **577**, 410–415 (2020).
54. Campbell, C. et al. Bacterial metabolism of bile acids promotes generation of peripheral regulatory T cells. *Nature* **581**, 475–479 (2020).
55. Einarsson, C., Hillebrant, C. G. & Axelson, M. Effects of treatment with deoxycholic acid and chenodeoxycholic acid on the hepatic synthesis of cholesterol and bile acids in healthy subjects. *Hepatology* **33**, 1189–1193 (2001).
56. Li, C. et al. Farnesoid X receptor agonists as therapeutic target for cardiometabolic diseases. *Front. Pharmacol.* **11**, 1247 (2020).
57. Ali, A. H., Carey, E. J. & Lindor, K. D. Recent advances in the development of farnesoid X receptor agonists. *Ann. Transl. Med.* **3**, 5 (2015).
58. Ferrell, J. M. & Chiang, J. Y. L. Understanding bile acid signaling in diabetes: from pathophysiology to therapeutic targets. *Diabetes Metab. J.* **43**, 257–272 (2019).
59. Li, T. & Apte, U. Bile acid metabolism and signaling in cholestasis, inflammation, and cancer. *Adv. Pharmacol.* **74**, 263–302 (2015).
60. Mahanti, P. et al. Comparative metabolomics reveals endogenous ligands of DAF-12, a nuclear hormone receptor, regulating *C. elegans* development and lifespan. *Cell Metab.* **19**, 73–83 (2014).

JRI Live Cell Bank

David Artis[2,3,7,9], Randy Longman[2,3,7], Gregory F. Sonnenberg[2,3,7], Ellen Scherl[2,3], Robbyn Sockolow[2,3,11], Dana Lukin[2,3], Vinita Jacob[2], Laura Sahyoun[2], Michael Mintz[2], Thomas Ciecierega[2,11], Aliza Solomon[2,11], Arielle Bergman[2,11], Kimberley Chein[2,11], Elliott Gordon[2,11], Kenny Joselin Castro Ochoa[2,11], Lily Barash[2,11], Victoria Ribeiro de Godoy[2,3], Adriana Brcic-Susak[2,3], Dario Garone[2,3], Caitlin Mason[2], Chloe Scott[2,3] & Lexi Tempera[2,3]

[11]Department of Pediatrics, Division of Gastroenterology, Hepatology, & Nutrition, Weill Cornell Medicine, Cornell University, New York, NY, USA.

Methods

Mice

C57BL/6 (000664, Jax) and *Nr1h4*$^{-/-}$ (007214, Jax) mice were originally purchased from The Jackson Laboratories and bred at Weill Cornell Medicine (WCM). *Vnn1*$^{-/-}$ mice[61] were bred at the Yale School of Medicine (a gift from P. Nasquet and R. Medzhitov). Germ-free C57BL/6J mice were bred and housed in flexible PVC isolators (Park Bioservices) at the WCM. Gnotobiotic mice were maintained in Sentry sealed positive pressure cages (SPP) for the duration of the experiments. All other mice were maintained under specific pathogen-free condition. All mice used were between 6 and 12 weeks of age, age and sex matched for each experiment, maintained on a 12-h light–dark cycle, an average ambient temperature of 21 °C and an average humidity of 48%, and provided food and water ad libitum. When studying the effects of dietary fibre[32], mice were given an inulin fibre diet (D16052309, Research Diets) supplemented with 30% fibre (26% inulin and 4% cellulose) or a calorie-matched control diet (D12450J-1.5, Research Diets) containing 4.7% cellulose. The duration of the fibre dietary intervention was 2 weeks unless otherwise stated. For the experimental model of hypercholestaeremia, mice were given a HCD (C23041301, Research Diets) supplemented with 1% cholesterol or standard mouse chow. The duration of the high-cholesterol dietary intervention was 4 weeks. All protocols were approved by the WCM Institutional Animal Care and Use Committees, and all mice were used in accordance of governmental and institutional guidelines for animal welfare.

Antibiotic treatment

Mice were provided autoclaved drinking water supplemented with a cocktail of broad-spectrum antibiotics as previously described[62]: ampicillin (0.5 mg ml^{-1}, Santa Cruz), gentamicin (0.5 mg ml^{-1}, Gemini Bio Products), metronidazole (0.5 mg ml^{-1}, Sigma), neomycin (0.5 mg ml^{-1}, Sigma), vancomycin (0.25 mg ml^{-1}, Chem-Impex International) and saccharin (4 mg ml^{-1}, Sweet'N Low, Cumberland Packing). Mice in the control group were provided with autoclaved drinking water supplemented with saccharin alone. Saccharin was added to make the antibiotic cocktail more palatable. Antibiotic treatment was started 2 weeks before the experiments and continued for the duration of the experiments with antibiotic and saccharin only control water replaced weekly.

Tissue collection and processing

Mice were euthanized by CO_2 narcosis according to institutional policies. Just before euthanasia, faecal samples were collected and frozen on dry ice. After euthanasia, whole blood was collected by subxiphoid cardiac puncture using a 1-ml syringe fitted with a 25 G × 5/8″ needle (both BD). Blood was immediately transferred to a SST Microtainer tube (BD) and allowed to clot for 30 min before centrifugation according to the manufacturer's instructions. Serum was then collected, transferred to a new tube and frozen on dry ice. After blood collection, animals were perfused through the left ventricle with 20 ml of ice-cold Ca^{2+}–Mg^{2+}-free DPBS (Corning) to flush the remaining vascular contents. Liver and ileum samples were then collected and either snap frozen on dry ice for metabolomics or placed into RNAprotect (Qiagen) for RNA extraction.

Human serum samples

Serum samples were obtained from a cohort previously described[63]. The original study protocol was approved by the Duke Health Institutional Review Board at Duke University under protocol number Pro00093322, and registered on ClinicalTrials.gov with the identified number NCT04055246. Informed consent was obtained from all participants.

Human FMT

For FMT studies, donor faecal samples were collected from healthy participants and resuspended in PBS with 10% glycerol in an anaerobic chamber[64]. Samples were obtained following Institutional Review Board-approved protocols from the JRI IBD Live Cell Bank Consortium at WCM, and informed consent was obtained from all participants. Faecal suspensions from individual donors were administered to recipient germ-free mice by oral gavage (100 µl per mouse). Transplanted animals were maintained in sterile isocages for 2–4 weeks. Animals were evaluated for successful transplantation by comparing 16S sequencing between human donors and recipient mice.

Metabolite extraction from the mouse liver, small intestine and caecum

Intact mouse liver was frozen and stored at −80 °C before processing. Frozen tissues were crushed and grinded using a pre-chilled mortar and pestle. Dry ice was added to a mortar and pestle throughout the homogenization process to prevent tissues from thawing. The resulting powdered samples were sonicated for 1 min with 5 ml methanol in 20-ml glass scintillation vials at a ratio with 10 µl solvent per mg, followed by another 10 min of vigorous stirring. Extracts were pelleted at 5,000*g* for 5 min, and supernatants were transferred to another 20-ml glass vials. Remaining pellets were further extracted with another 10 min of vigorous stirring in 5 ml ethanol. The supernatants were combined and then dried in a SpeedVac (Thermo Fisher Scientific) vacuum concentrator. Dried materials were resuspended in 300 µl of methanol. Samples were pelleted at 5,000*g* for 5 min, and clarified extracts were transferred to fresh HPLC vials and stored at −20 °C until analysis.

Metabolite extraction from mouse serum samples

Of methanol, 800 µl was added to 200 µl of serum in 1.7-ml Eppendorf tubes. The tubes were sonicated for 1 min followed by another 10 min of vigorous stirring. Extracts were pelleted at 5,000*g* for 5 min, and supernatants were transferred to 2-ml HPLC vials. Remaining pellets were further extracted with another 10 min of vigorous stirring in 500 µl ethanol. Extracts were pelleted at 5,000*g* for 5 min, and the combined supernatants were dried in a SpeedVac (Thermo Fisher Scientific) vacuum concentrator. Samples were resuspended in 100 µl of methanol and pelleted at 5,000*g* for 5 min. Clarified extracts were transferred to fresh HPLC vials and stored at −20 °C until analysis.

Metabolite extraction from mouse faeces

Of methanol, 600 µl was added to 30 mg of faeces in 1.7-ml Eppendorf tubes. The tubes were sonicated for 1 min, followed by another 10 min of vigorous stirring. Extracts were pelleted at 5,000*g* for 5 min, and supernatants were transferred to 2-ml HPLC vials. Remaining pellets were further extracted with another 10 min of vigorous stirring in 600 µl ethanol. Extracts were pelleted at 5,000*g* for 5 min, and the combined supernatants were then dried in a SpeedVac (Thermo Fisher Scientific) vacuum concentrator. Samples were then resuspended in 100 µl of methanol and pelleted at 5,000*g* for 5 min, and the clarified extracts were transferred to fresh HPLC vials and stored at −20 °C until analysis.

Analytical methods and equipment overview

For mass spectrometry, high-resolution light chromatography–mass spectrometry was performed on a Thermo Fischer Scientific Vanquish UHPLC system coupled with a Thermo Q-Exactive HF hybrid quadrupole-orbitrap high-resolution mass spectrometer equipped with a HESI ion source. Metabolites were separated using acetonitrile containing 0.1% formic acid (organic phase) and 0.1% formic acid in water (aqueous phase) as solvents on a Thermo Fisher Scientific Hypersil GOLD C18 column (150 mm × 2.1 mm, particle size of 1.8 µm). The gradient started at 1% organic for 3 min after injection and increased linearly to 100% organic over 20 min, then 100% organic for 5 min, and down to 1% organic for 3 min at a flow rate of 0.5 ml min^{-1}. The mass spectrometer parameters were: spray voltage of 3.5 kV, capillary temperature of 380 °C, probe heater temperature of 400 °C; 60 sheath flow rate, 20 auxiliary flow rate and 1 spare gas; and S-lens RF level of 50,

resolution of 240,000, automatic gain control (AGC) target of 3×10^6. The instrument was calibrated weekly with positive and negative ion calibration solutions (Thermo Fisher). Each sample was analysed in negative and positive ionization modes using a m/z range of 100–800. NMR spectroscopy was performed on a Varian INOVA 600 MHz NMR spectrometer (600 MHz ^{1}H reference frequency, 151 MHz for ^{13}C) equipped with an HCN indirect-detection probe. Non-gradient phase-cycled dqfCOSY spectra were acquired using the following parameters: 0.6 s acquisition time, 400–600 complex increments and 8, 16 or 32 scans per increment. HSQC and HMBC spectra were acquired with these parameters: 0.25 s acquisition time, 200–500 increments and 8–64 scans per increment. ^{1}H, ^{13}C-HMBC spectra were optimized for $J_{H,C}$ = 6 Hz. HSQC spectra were acquired with or without decoupling. NMR spectra were processed and baseline corrected using MestreLabs MNOVA software packages.

Feature detection and characterization

Liquid chromatography–mass spectrometry RAW files for all serum samples were converted to mzXML format (centroid mode) using MSconvert (ProteoWizard version 3.0.18250-994311be0), followed by analysis using the XCMS analysis feature in Metaboseek (version 0.9.7; https://metaboseek.com)[31] based on the centWave XCMS algorithm to extract features[65,66]. Peak detection values were set as: 4 ppm, 3–20 peakwidth, 3 snthresh, 3 and 100 prefilter, FALSE fitgauss, 1 integrate, TRUE firstBaselineCheck, 0 noise, wMean mzCenterFun and −0.005 mzdiff. XCMS feature grouping values were set as: 0.2 minfrac, 2 bw, 0.002 mzwid, 500 max, 1 minsamp and FALSE usegroup. Metaboseek peak filling values were set as: 5 ppm_m, 5 rtw and TRUE rtrange. Resulting tables of all detected features were then processed with the Metaboseek data explorer. To remove background-derived features, we first applied filters that only retained entries with a retention time window of 1–20 min, and then applied maximum intensity (at least one repeat of more than 10,000) and peak quality (more than 0.98) thresholds, as calculated by Metaboseek[31]. To select differential features, we applied a filter retaining entries with peak area ratios more than fivefold reduced or fivefold increased in germ-free mice compared with SPF mice, as calculated by Metaboseek[31]. We manually curated the resulting list to remove false-positive entries, that is, features that upon manual inspection of raw data were not differential. For verified differential features, we examined elution profiles, isotope patterns and MS1 spectra to find molecular ions and remove adducts, fragments and isotope peaks. Remaining masses were put on the inclusion list for MS/MS (ddMS2) characterization. Positive and negative ionization mode data were processed separately. To acquire MS2 spectra, we ran a top-10 data-dependent MS2 method on the Thermo Q-exactive-HF mass spectrometer with MS1 resolution of 60,000, AGC target of 1×10^6, maximum injection time of 50 ms, MS2 resolution of 45,000, AGC target of 5×10^5, maximum injection time of 80 ms, isolation window of 1.0 m/z, stepped normalized collision energy of 10 and 30 for positive and negative ionization mode, respectively, and dynamic exclusion of 3 s. To focus on BAs and BA derivatives, we selectively analysed differential features whose MS2 spectra contained fragment ions for complete 24-carbon backbones (Supplementary Table 1).

MS2-based molecular networking

A MS2 molecular network was created using Metaboseek (version 0.9.7)[31] and visualized in Cytoscape (version 3.9.1)[67]. Features were matched with their respective MS2 scan within an m/z window of 5 ppm and a retention time window of 15 s, using the MS2scans function. To construct the molecular network, tolerance of the fragment peaks was set to m/z of 0.001 or 3 ppm and the minimum number of peaks was set to 1, with a 2% noise level. Once the network was constructed, a cosine value of 0.7 was used, the number of possible connections was constrained to 6 and the maximum cluster size was restricted to 200 for both negative ion mode and positive ion mode.

General procedures for chemical syntheses

Unless noted otherwise, all chemicals and reagents were purchased from Sigma-Aldrich. Solutions and solvents sensitive to moisture and oxygen were transferred via standard syringe and cannula techniques. Acetic acid, acetonitrile, dichloromethane and methanol used for chromatography and as a reagent or solvent were purchased from Fisher Scientific. Flash chromatography was performed using Teledyne Isco CombiFlash systems using Teledyne Isco RediSep Rf silica and C18 columns. See Supplementary Information for synthetic schemes, protocols, NMR spectroscopic data and spectra. NMR spectra were processed and baseline corrected using Mestrelab Mnova (version 14.2.1-27684) software packages.

Generation of correlation plots

Correlation plots were created using GraphPad Prism (version 10.2.0). The R^2 values from non-linear regression analyses were calculated using GraphPad Prism and used as a measure of goodness of fit. Quantification was performed via integration in Xcalibur 4.1 Qualbrowser (version 4.1.31.9, Thermo Scientific). Cholic acid, ω-muricholic acid, α-muricholic acid, β-muricholic acid, chenodeoxycholic acid, ursodeoxycholic acid, 7-ketodeoxycholic acid and deoxycholic acid were quantified and included in 'total free BAs', and their corresponding MCY, MCYO and MCYO2 conjugates were quantified and included in 'total BA–MCYs'. The average total amount of free BAs in groups of SPF mice used as control for different experiments was used to normalize data for total free BAs and total BA–MCYs for all groups.

Administration of metabolites

Taurine-d_4 (Cambridge isotope laboratories) dissolved in saline was delivered intraperitoneally daily at a rate of 100 mg kg^{-1} body weight in a volume of 100 µl. L-Cysteine-3,3-d_2 was delivered at a rate of 100 mg kg^{-1} body weight per day by oral gavage. The metabolites were administered for a duration of 5 days. CDCA–MCY or CDCA–d_5–MCY (dissolved in DMSO and further diluted in corn oil) was delivered by oral gavage at a rate of 50 mg kg^{-1} body weight per day in a volume of 100 µl for 2 weeks. The vehicle control group received DMSO and corn oil. In the HCD model, mice were treated under the same conditions for a total of 6 weeks (2 weeks before initiation of the HCD, and throughout the diet exposure period. In some experiments, a tenfold lower dose (5 mg kg^{-1}) was used for CDCA–MCY or CDCA–d_5–MCY.

VNN1 in vitro assays with pantetheine derivatives

Reactions were initiated by adding 10 µl of 0.02 µM recombinant human ΔN490aa VNN1 protein (Sino Biological; with a C-terminal poly His tag, reconstituted in PBS pH 7.0) to 10 µl pantetheine (or CA–pantetheine derivative) diluted with PBS (pH 7.0) so that the final concentrations of pantetheine (derivative) were 20, 40, 80, 160, 320 and 640 µM. The mixtures were quenched with 180 µl methanol after allowing the reaction to proceed for 15 min at 37 °C and directly injected for HPLC–HRMS analysis. The HPLC–HRMS analysis method was the same as described in the 'Analytical methods and equipment overview' section, except that a shorter HPLC method was used. The gradient was as follows: started at 1% organic for 2 min, linearly increasing to 98% organic over 2.5 min, then 98% organic for 2.5 min, shifting back to 1% organic in 0.1 min until 9 min. Pantothenic acid was detected in ESI$^+$ mode at m/z 220.1180 ± 5 ppm. Initial velocity of each reaction was calculated by dividing the concentration of produced pantothenic acid determined using a standard curve of D-calcium pantothenate (Acros Organics) for 15 min. Michaelis–Menten kinetic regression was performed using GraphPad Prism (version 10.2.0).

Analysis of CDCA–d_5–MCY metabolism in vivo

Use of the Label Finder tool in Metaboseek[31] facilitated untargeted detection of any d_4-labelled (Δm/z of 4.0251) and d_5-labelled (Δm/z of

5.0314) metabolites derived from administered CDCA–d_5–MCY in SPF, germ-free or ABX mice monocolonized with *B. ovatus* strains. CDCA–d_5–MCY was administered by oral gavage at a rate of 50 mg kg^{-1} body weight as described above. The vehicle control group received DMSO and corn oil. Peak detection values were set as follows: retention time (RT) tolerance of 3 s, peak width tolerance factor of 10, *m/z* tolerance of 5 ppm, RT window of 5 s, minimum intensity ratio of unlabelled peak-to-labelled peak in unlabelled samples of 10, and maximum intensity ratio of unlabelled peak-to-labelled peak in unlabelled samples of 5. Resulting tables of all detected features were then processed with the Metaboseek data explorer. To remove background-derived features, we first applied filters that only retained entries with a retention time window of 5–20 min and *m/z* between 300 and 600, and then applied a peak quality (more than 0.98) threshold, as calculated by Metaboseek[31]. The resulting table was then processed with Microsoft Excel to generate bubble plots[68].

DiscoverX assay for activity against human FXR

Tauro-β-muricholic acid (Sigma) and synthetic MCY conjugates including CA–MCY, CA–MCYO, CDCA–MCY and βMCA–MCY were tested in a cell-based assay on FXR with known ligands, GW4064 and DY268, in both agonist (item #86-0003P-2453AG) and antagonist (item #86-0003P-2453AN) modes, respectively (assays were performed by DiscoverX/Eurofins).

CHO-K1 cells tested negative for mycoplasma and were expanded from freezer stocks according to standard procedures. Cells were not authenticated. Cells were seeded in a total volume of 20 µl into white-walled, 384-well microplates and incubated at 37 °C for the appropriate time before testing. Assay media contained charcoal-dextran-filtered serum to reduce the level of hormones present. For agonist determination, cells were incubated with sample to induce response. Intermediate dilution of sample stocks was performed to generate 5X sample in assay buffer. Of the 5X sample, 5 µl was added to cells and incubated at 37 °C or room temperature for 3–16 h. Final assay vehicle concentration was 1 µl. For antagonist determination, cells were pre-incubated with antagonist followed by agonist challenge, GW4064 (0.37 µM, EC_{80}), obeticholic acid (25 µM) or CDCA (25 µM). Intermediate dilution of sample stocks was performed to generate 5X sample in assay buffer. Of the 5X sample, 5 µl was added to cells and incubated at 37 °C or room temperature for 60 min. Vehicle concentration was 1%. Of the 6X EC_{80} agonist in assay buffer, 5 µl was added to the cells and incubated at 37 °C or room temperature for 3–16 h. Compound activity was detected by chemiluminescent signals indicating ligand binding that induces FXR activation, translocation and co-activator interaction. For signal detection, the assay signal was generated through a single addition of 12.5 µl or 15 µl (50% v/v) of PathHunter Detection reagent cocktail, followed by a 1-h incubation at room temperature. Microplates were read following signal generation with a PerkinElmer Envision instrument for chemiluminescent signal detection. The agonist mode measures the percentage activity relative to the maximum value activated by GW4064 (100% activation)[45]. The antagonist mode measures the percentage activity relative to the maximum value activated by DY268 (100% activation). For agonist mode assays, the percentage activity was calculated using the following formula: activity (%) = 100 × (mean relative light unit (RLU) of test sample − mean RLU of vehicle control)/(mean maximum control ligand − mean RLU of vehicle control). For antagonist mode assays, the percentage inhibition was calculated using the following formula: inhibition (%) = 100 × (1 − (mean RLU of test sample − mean RLU of vehicle control)/(mean RLU of EC_{80} control − mean RLU of vehicle control).

DiscoverX assay for cell viability against human primary hepatocytes

Chenodeoxycholic acid (Sigma) and synthetic CDCA–MCYO were tested in a cell-based assay using human primary hepatocytes (assays were performed by DiscoverX/Eurofins, item 5137). Cryopreserved human hepatocytes were thawed and plated into collagen-coated 96-well plates in the Plating Medium (serum containing) at a density of 0.2 × 10^6 viable cells per millilitre. Hepatocytes were cultured at 37 °C and 5% CO_2 for 18–24 h. After 18–24 h of plating, the hepatocytes were incubated with the test compound in the incubation medium (serum free). Cell viability was measured by CellTiter-Glo (Promega) after 24-h compound incubation. Compounds were tested in duplicates at multiple concentrations (0.15, 0.45, 1.5, 4.5, 15, 45, 150 and 450 µM) for IC_{50} determinations. Chlorpromazine was tested at multiple concentrations to obtain an IC_{50} value. The final DMSO concentration was 0.5%. For data analysis, the percent of control activity was calculated by comparing the readings in the presence of the test compound to the vehicle control. IC_{50} values (concentration causing a half-maximal inhibition of the control value) were determined by non-linear regression analysis of the concentration response curves using the Hill equation.

Quantitative real-time PCR and ELISA

Total RNA was isolated from tissues using the RNeasy Plus mini kit (Qiagen), and cDNA was synthesized using the High-Capacity cDNA Reverse Transcription Kit with Multiscribe Reverse Transcriptase (Thermo Fisher), according to the protocol provided by the manufacturer. Quantitative PCRs were set up using the Power SYBR Green PCR Master Mix (Thermo Fisher) and run on a QuantStudio 6 Flex Real-Time PCR System (Applied Biosystems) using QuantStudio Real-Time PCR software (version 1.0). The primers are listed[43] in Supplementary Table 5. FGF15 ELISA was performed using the mouse FGF15 ELISA Kit (LSBio) as per the manufacturer's protocol.

Histological analysis

After euthanasia and perfusion, a single lobe of the liver was carefully removed and fresh-frozen in optimal cutting temperature using a dry-ice–isobutane bath. Tissue blocks were stored at −80 °C until sectioning. Sectioning was performed on a Leica CM3050S cryostat to a thickness of 10 µm and collected on Superfrost Plus Slides (VWR). Sections were then again stored at −80 °C before staining. For oil red O staining, slides were stained according to the manufacturer's instructions using an Oil Red O Stain Kit (Abcam), omitting the nuclear counterstaining step. Stained slides were imaged on a Nikon Eclipse Ti microscope using a 20× Plan APO 0.45 NA lens using identical illumination and detection settings. Four random 20× fields were captured per section in two separate tissue sections for a total of eight fields per animal. The total oil red O pixel area in each 20× field was calculated using a custom Fiji script[69]. The pixel area was then averaged over the eight captured sections and converted to area in µm^2 using the known pixel:µm calibration of the imaging system.

Monocolonization of germ-free mice

WT or mutant *B. ovatus* strains previously generated[32] were grown in a TYGB/Mega medium at 37 °C overnight inside an anaerobic chamber. Germ-free mice were monocolonized by oral gavage of the bacterial culture (200 µl; approximately 1 × 10^7 colony-forming units (CFU)) and maintained in Sentry-sealed positive pressure cages (SPP) for the duration of the experiments. The level of colonization was determined by quantifying the bacterial load in mouse faecal pellets (CFU per gram of faeces). In brief, approximately 5 mg of faecal material was resuspended in 200 µl of pre-reduced Gibco PBS buffer (pH 7.4). Then, a tenfold serial dilution (to 10^{-4}) was made in the same buffer on a 96-well plate, and 50 µl from each 10^{-4}-diluted well was plated onto anaerobically pre-reduced TSAB agar at 37 °C. After 24 h, colonies appeared and the CFU for faecal samples collected from WT and mutant colonized germ-free mice were calculated after normalizing to faecal weight.

In vitro experiments with gut bacteria and mouse faecal suspensions

Of *Enterococcus faecalis*, *Lactiplantibacillus plantarum*, *Ruminococcus gnavus*, *Enterocloster bolteae* or *Clostridium scindens* (optical density at 600 nm (OD_{600}) of 0.5–0.6), 50 µM was inoculated with 100 µM of CA–MCY, CA–MCYO or CA–MCYO2 in 450 µl of reinforced clostridial medium and incubated at 37 °C for 48 h. Faecal samples were collected from three SPF mice in different cages. Approximately 50 mg of mouse faecal sample was homogenized in 4 ml brain heart infusion medium and incubated at 37 °C for 24 h. Subsequently, passaging was then performed in 15-ml tubes at a dilution of 1:4 every 24 h for a total of two passages. Of the passaged bacteria community (OD_{600} 0.5–0.6), 50 µl was inoculated with 100 µM of CA–MCY, CA–MCYO or CA–MCYO2 in 450 µl of brain heart infusion medium and incubated at 37 °C for 48 h. After in vitro culture, 200 µl of culture was added to 300 µl ice-cold methanol at a final concentration of 60% methanol followed by overnight incubation at 4 °C. Extracted metabolites were stored at −80 °C. Before the mass spectrometry analysis, samples were spun down at 12,000*g* for 5 min, and the supernatant was transferred to 96-well plates followed by dilution 1:1 (v:v) in 50% methanol containing 2.5 µg ml^{-1} phenolsulfonphthalein for liquid chromatography–tandem mass spectrometry analysis. Detailed methods for the comparative metabolomic analyses have been previously described[42]. In brief, raw files were converted to mzXML format via GNPS Vendor Conversion, and the Global Natural Products Social Molecular Networking Database (GNPS, University of California at San Diego) was submitted for spectral identification.

Statistical analysis

All statistical analysis was performed with GraphPad Prism (version 10.2.0) or Metaboseek (version 0.9.7). The statistical details of experiments can be found in the figure legends. Reported *n* values are the total samples per group. The *P* values of datasets were determined by unpaired two-tailed Student's *t*-test with Welch's correction, unless specified otherwise. Normal distribution was assumed. If equal variances between two groups could not be assumed, Welch's correction was performed. No statistical methods were used to predetermine sample size. The experiments were not randomized, and the investigators were not blinded to allocation during experiments and outcome assessment. No animals were excluded from the analysis unless clearly indicated. The entity *n* represents biologically independent samples and not technical replicates unless specified otherwise. Error bars show the s.e.m. unless specified otherwise.

Reporting summary

Further information on research design is available in the Nature Portfolio Reporting Summary linked to this article.

Data availability

Source data for Figs. 2–5 and Extended Data Figs. 2, 3 and 5–12 are provided with this paper. Raw sequencing reads were uploaded to the Sequence Read Archive under accession number BioProject PRJNA761331, and mass spectrometry data for all mouse metabolome samples analysed in this study are available on the GNPS website (https://massive.ucsd.edu) under MassIVE ID number MSV000090974. Source data are provided with this paper.

Code availability

The custom Fiji script used for the analysis of liver lipid accumulation imaging is available on Zenodo[69] (https://doi.org/10.5281/zenodo.14031611).

61. Pitari, G. et al. Pantetheinase activity of membrane-bound vanin-1: lack of free cysteamine in tissues of vanin-1 deficient mice. *FEBS Lett.* **483**, 149–154 (2000).
62. Hepworth, M. R. et al. Immune tolerance. Group 3 innate lymphoid cells mediate intestinal selection of commensal bacteria-specific $CD4^+$ T cells. *Science* **348**, 1031–1035 (2015).
63. Letourneau, J. et al. Ecological memory of prior nutrient exposure in the human gut microbiome. *ISME J.* **16**, 2479–2490 (2022).
64. Goc, J. et al. Dysregulation of ILC3s unleashes progression and immunotherapy resistance in colon cancer. *Cell* **184**, 5015–5030.e16 (2021).
65. Tautenhahn, R., Bottcher, C. & Neumann, S. Highly sensitive feature detection for high resolution LC/MS. *BMC Bioinformatics* **9**, 504 (2008).
66. Wang, M. et al. Sharing and community curation of mass spectrometry data with Global Natural Products Social Molecular Networking. *Nat. Biotechnol.* **34**, 828–837 (2016).
67. Shannon, P. et al. Cytoscape: a software environment for integrated models of biomolecular interaction networks. *Genome Res.* **13**, 2498–2504 (2003).
68. Zhang, B. et al. Acylspermidines are conserved mitochondrial sirtuin-dependent metabolites. *Nat. Chem. Biol.* **20**, 812–822 (2024).
69. Parkhurst, C. Fiji oil red O macro. *Zenodo* https://doi.org/10.5281/zenodo.14031611 (2024).

Acknowledgements We thank members of the Schroeder and Artis laboratories for discussion and critical reading of the manuscript; B. Fox for assistance with mass spectrometry; and all contributing members of the JRI IBD Live Cell Bank consortium, which is supported by the Jill Roberts Institute for Research in IBD, the Jill Roberts Center for IBD, Cure for IBD, the Rosanne H. Silbermann Foundation, the Sanders Family, and the WCM Division of Pediatric Gastroenterology and Nutrition. The schematics in Fig. 1a were created using BioRender (https://biorender.com). All chemical structures were created with ChemDraw. This work was supported by the Crohn's & Colitis Foundation (to M.A.), the Thomas C. King Pulmonary Fellowship, the WCM Fund for the Future, the Sackler Brain and Spine Institute Research Grant, and a Brain and Behavior Research Foundation (NARSAD) Young Investigator Award (all to C.N.P.), Office of Naval Research grant N00014-18-1-2616 (to L.A.D.), the Howard Hughes Medical Institute (to F.C.S.), Kenneth Rainin Foundation and the W. M. Keck Foundation (all to C.-J.G.), The Global Grants for Gut Health co-supported by Yakult and Nature Research (to R.A.Q.), the AGA Research Foundation, the WCM-RAPP Initiative, Cure for IBD, the Jill Roberts Institute for Research in IBD, the Kenneth Rainin Foundation, the Sanders Family Foundation, the Rosanne H. Silbermann Foundation, the Glenn Greenberg and Linda Vester Foundation, the Allen Discovery Center Program, a Paul G. Allen Frontiers Group advised program of the Paul G. Allen Family Foundation (all to D.A.), and the US National Institutes of Health (K99AI173660 to M.A., K08MH130773 and NIAID Mucosal Immunology Studies Team Young Investigator Award to C.N.P., GM131877 to F.C.S., DK116187 to L.A.D., DK140854 to R.A.Q., DP2 HD101401 and DK135816 to C.-J.G., and DK126871, AI151599, AI095466, AI095608, AR070116, AI172027 and DK132244 to D.A.).

Author contributions D.A. and F.C.S. supervised the study. T.H.W. carried out the metabolomics and chemical synthesis and analysed most of the data. C.N.P. and M.A. conducted all animal experiments. W.-B.J. and C.-J.G. provided the bacterial strains and helped with the monocolonization experiments. S.K., E.H. and I.C.M. helped with the mouse experiments and various other assays. B.Z. assisted with the metabolomic analyses and conducted the VNN1 assays. J.L. and L.A.D. provided the human samples. Y.F., D.V.G. and R.A.Q. provided the *Baat*-knockout mouse metabolome samples and data analysis, as well as microbial analyses. The JRI Live Cell Bank contributed to clinical sample acquisition, annotation, processing and evaluation. T.H.W., M.A., C.N.P., D.A. and F.C.S. analysed the data and wrote the manuscript with input from all co-authors.

Competing interests D.A. has contributed to scientific advisory boards at Pfizer, Takeda, Nemagene and the Kenneth Rainin Foundation. F.C.S. is a cofounder of Ascribe Bioscience and Holoclara Inc., and a member of the scientific advisory board of Hexagon Bio. The other authors declare no competing interests.

Additional information

Supplementary information The online version contains supplementary material available at https://doi.org/10.1038/s41586-024-08379-9.

Correspondence and requests for materials should be addressed to David Artis or Frank C. Schroeder.

Peer review information *Nature* thanks the anonymous reviewers for their contribution to the peer review of this work. Peer reviewer reports are available.

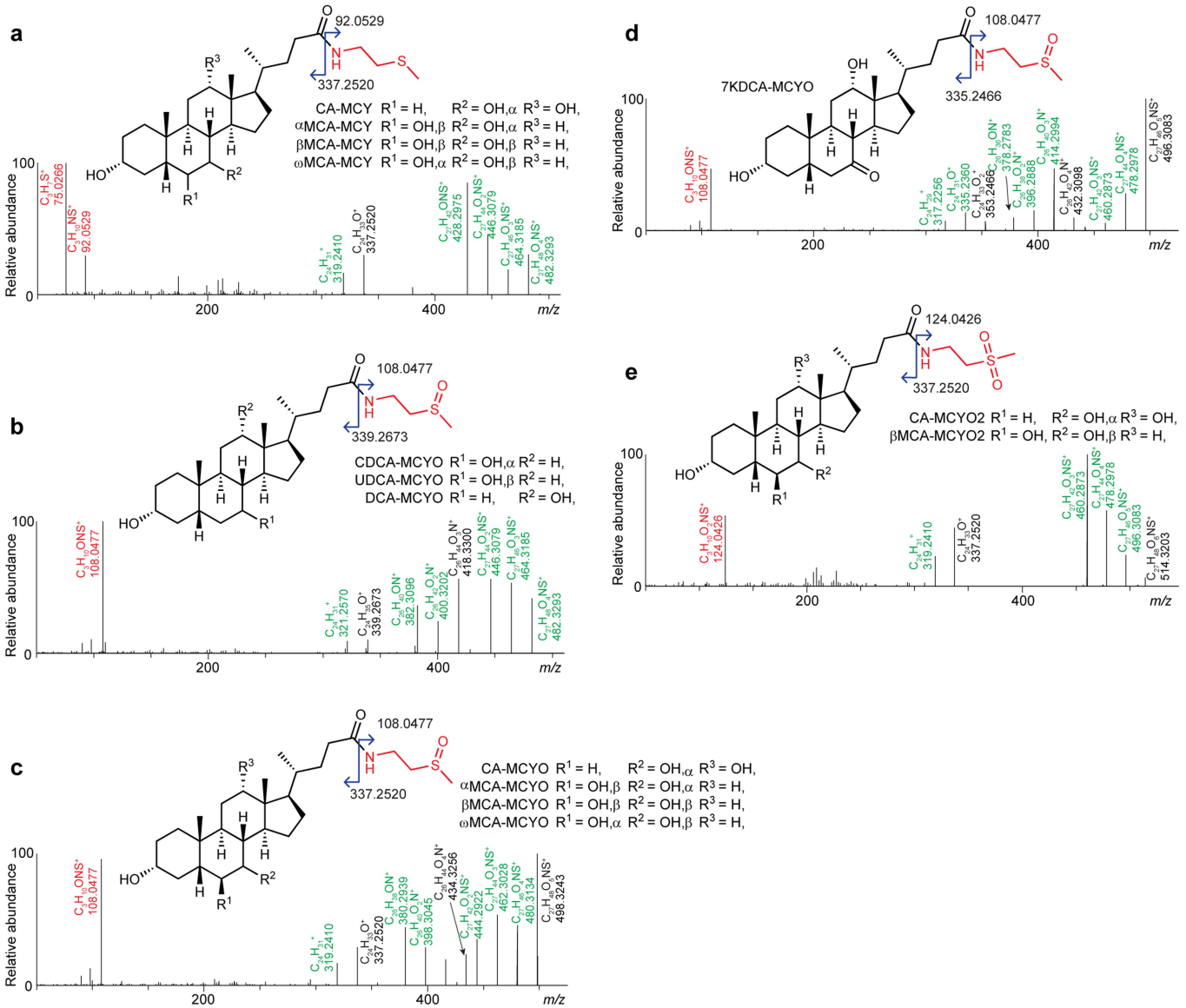

Extended Data Fig. 1 | MS2 spectra of MCY conjugates of BAs. a-e, MS2 spectra of CA-MCY (**a**), CDCA-MCYO (**b**), CA-MCYO (**c**), 7KDCA-MCYO (**d**), and CA-MCYO2 (**e**). The listed BA-MCY conjugates in each panel produced MS2 spectra very similar to the shown examples. Blue arrows indicate inferred fragmentation. MS2 fragments and structure parts highlighted in red represent MCY groups. Green fragments are derived from water loss.

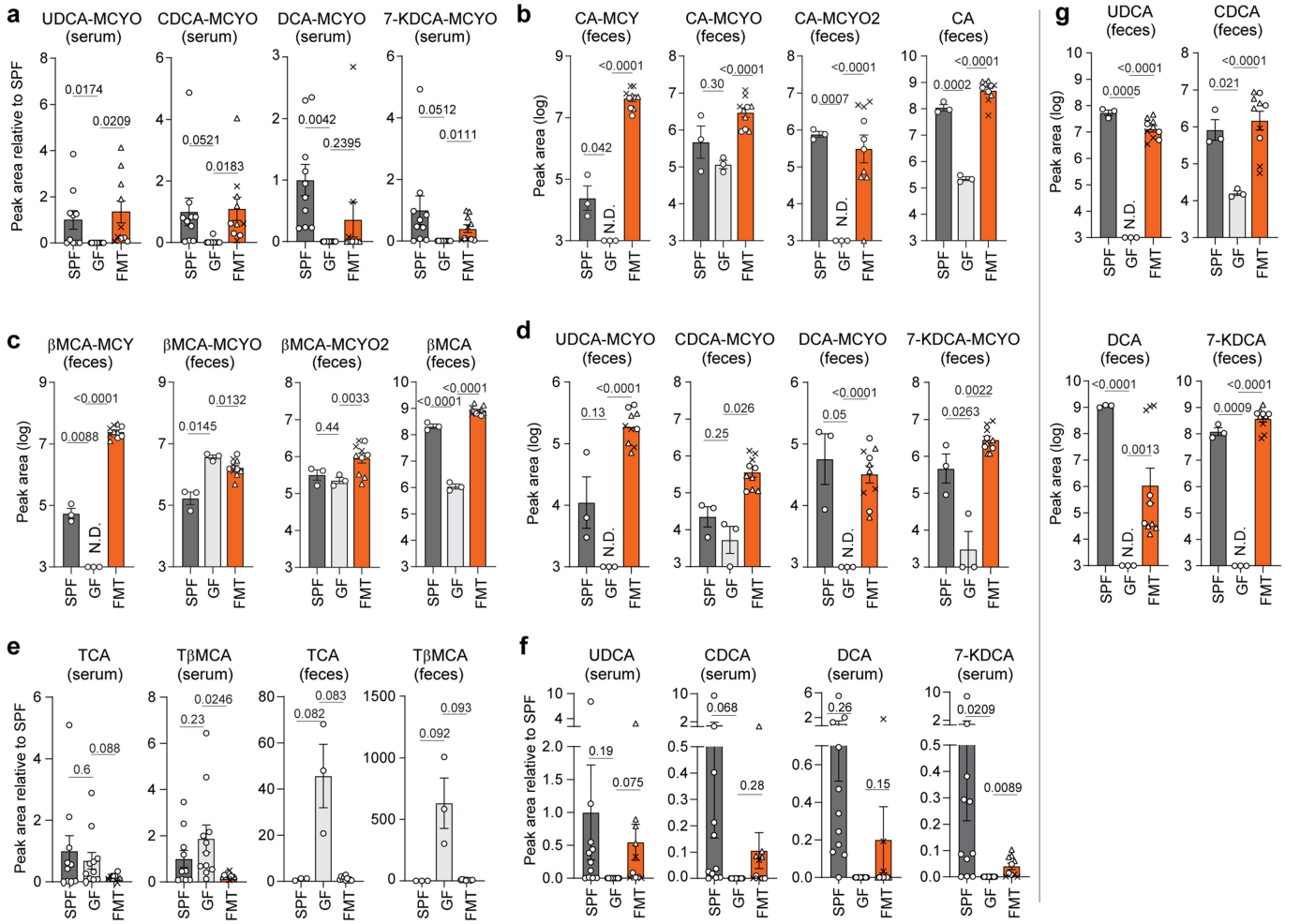

Extended Data Fig. 2 | Microbiota dependent production of BA-taurine and BA-MCY conjugates. a, Relative abundances of BA-MCYO conjugates of less abundant BAs in serum of SPF (n = 11) and GF (n = 12), and mice that received FMT (n = 10, the three donors are represented by triangles, circles, and crosses, n = 3-4 for each donor). **b,c**, Relative abundances of CA-MCY conjugates (**b**) and βMCA-MCY conjugates (**c**) as well as the corresponding free BAs in feces of SPF mice (n = 3), GF mice (n = 3), and mice that received FMT (n = 10, the three donors are represented by triangles, circles, and crosses, n = 3-4 for each donor). N.D., not detected. **d**, Relative abundances of BA-MCYO conjugates of less abundant BAs in feces of SPF (n = 3) and GF (n = 3), and mice that received FMT (n = 10, the three donors are represented by triangles, circles, and crosses, n = 3-4 for each donor). **e**, Relative abundances of BA-taurine conjugates in serum or feces of SPF (n = 11 for serum and n = 3 for feces) and GF (n = 12 for serum and n = 3 for feces), and mice that received FMT (n = 10, the three donors are represented by triangles, circles, and crosses, n = 3-4 for each donor). **f**,**g**, Relative abundances of free BAs in serum (**f**) or feces (**g**) of SPF (n = 11 for serum and n = 3 for feces) and GF (n = 12 for serum and n = 3 for feces), and mice that received FMT (n = 10, the three donors are represented by triangles, circles, and crosses, n = 3-4 for each donor). Data are mean ± s.e.m. *P* values were calculated using unpaired two-sided Student's *t*-test with Welch's correction.

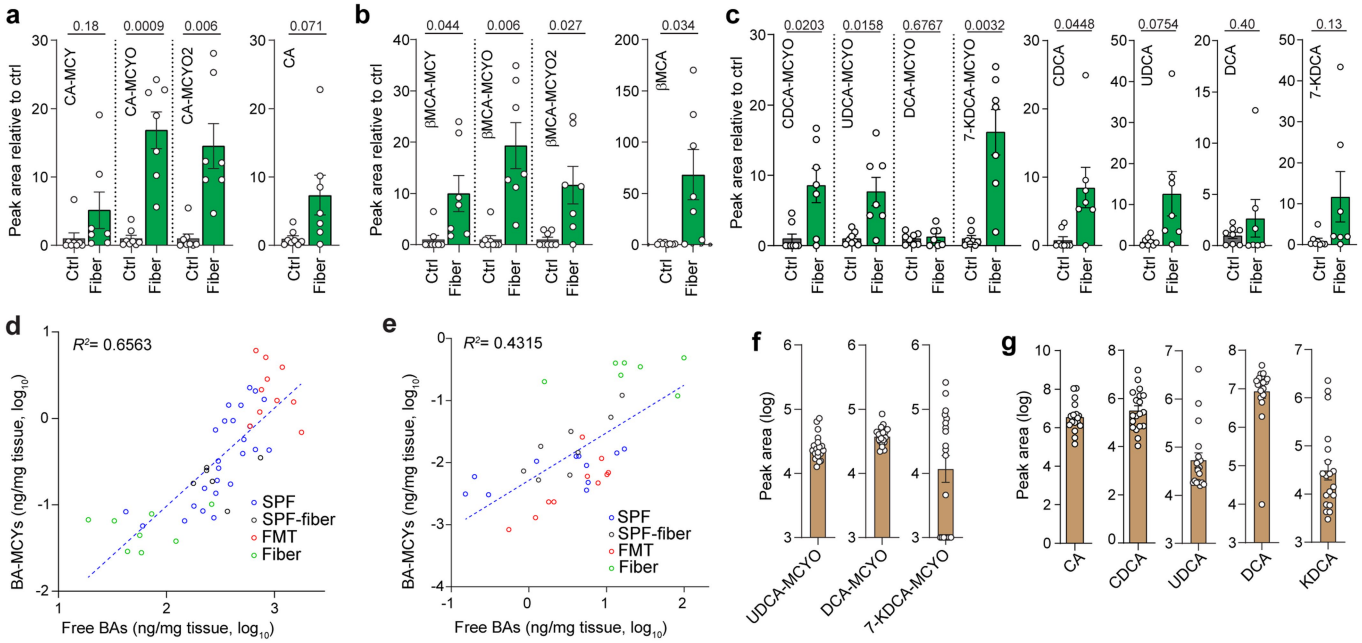

Extended Data Fig. 3 | Relationship between abundances of free BAs and BA-MCY conjugates. a,**b**, Relative abundances of CA-MCY (**a**) and βMCA-MCY conjugates (**b**) as well as corresponding free BAs in serum of mice fed control (n = 8) or inulin fiber diet (n = 7). **c**, Relative abundances of BA-MCYO conjugates as well as corresponding free BAs in serum of mice fed control (n = 8) or inulin fiber diet (n = 7). **d**, Relationship between abundances of free BAs and BA-MCY conjugates in feces of SPF mice used as control for the FMT study (n = 25), FMT mice (n = 10), SPF mice fed a control diet for the inulin fiber diet study (n = 6), and inulin fiber diet fed SPF mice (n = 8). **e**, Relationship between abundances of free BAs and BA-MCY conjugates in serum of SPF as control for the FMT study (n = 11), FMT mice (n = 10), SPF mice fed a control diet for the inulin fiber diet study (n = 8), and inulin fiber diet fed SPF mice (n = 7). **f**,**g**, Relative abundances of free BAs (**f**) and corresponding BA-MCY conjugates (**g**) in serum of human (n = 19). Data are mean ± s.e.m. *P* values were calculated using unpaired two-sided Student's *t*-test with Welch's correction.

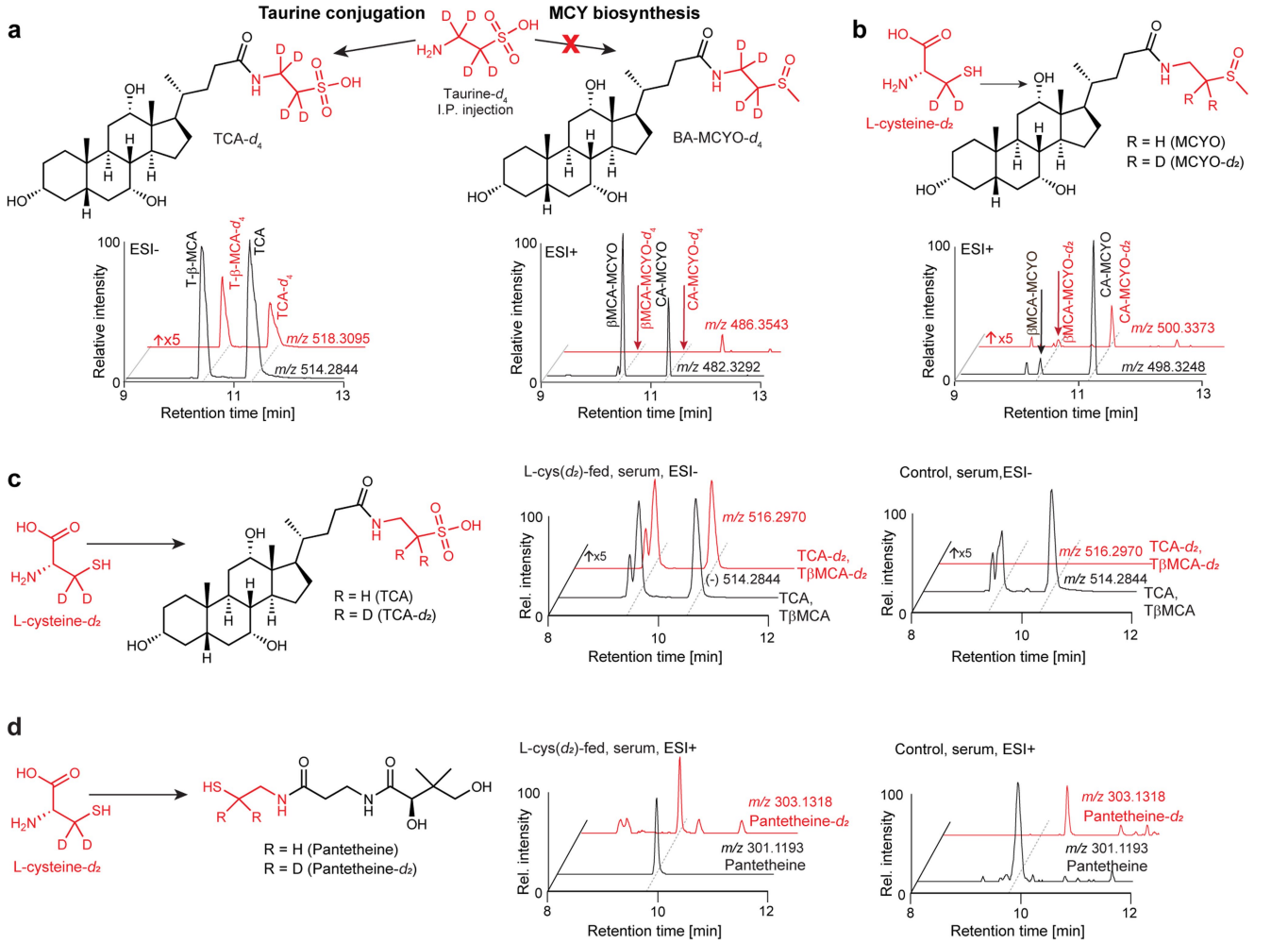

Extended Data Fig. 4 | Analysis of stable-isotope feeding experiments. **a**, Administration of taurine-d_4 in SPF mice resulted in deuterium incorporation in all detected taurine conjugates, but not in any MCY conjugates. Shown are EICs for the *m/z* of molecular ions of unlabeled (black) and deuterium-labeled versions (red) of the different conjugates in serum of mouse fed taurine-d_4. **b**, Administration of deuterium-labeled L-cysteine (L-cys-d_2) in SPF mice resulted in deuterium incorporation in the MCY conjugates of BAs. Shown are EICs for the *m/z* of the molecular ions of the unlabeled (black) and the deuterium-labeled versions of BA-MCY conjugates (red) detected in serum of mice fed L-cys-d_2. **c**,**d**, Administration of deuterium-labeled L-cysteine (L-cys-d_2) in SPF mice (see Fig. 2i) resulted in deuterium incorporation in taurine conjugates of BAs (**c**) and pantetheine (**d**). EICs for molecular ion peaks (black) and deuterium isotope peaks (red) of taurine conjugates of BAs (**c**) and pantetheine (**d**) in serum of mouse fed L-cys-d_2.

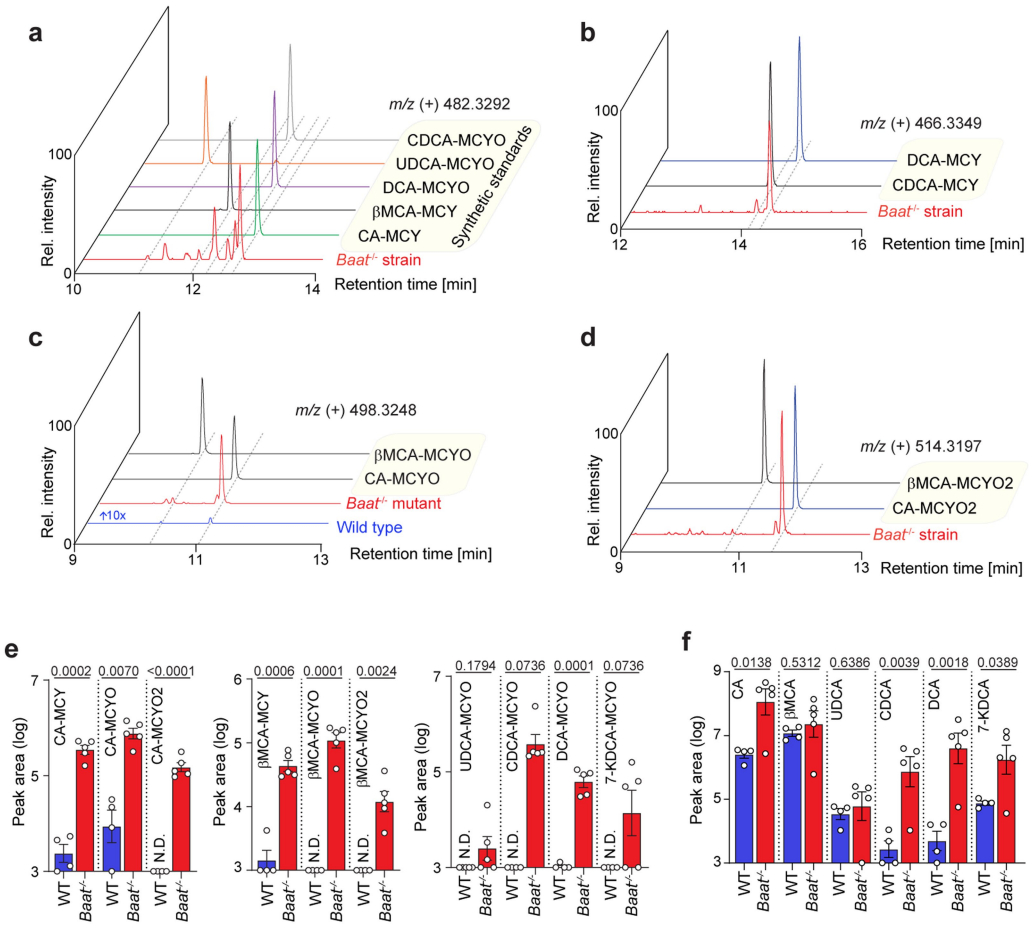

Extended Data Fig. 5 | Analysis of *Baat*$^{-/-}$ mice. a-d, Extracted ion chromatograms (EICs) of BA-MCY and BA-MCYO conjugates (**a**,**b**,**c**) and BA-MCYO2 conjugates (**d**) in liver of *Baat*$^{-/-}$ mice and comparison with synthetic standards analyzed in ESI + . **e**,**f**, Relative abundances of BA-MCY conjugates (**e**) and corresponding free BAs (**f**) in liver of WT (n = 4) or *Baat*$^{-/-}$ (n = 5) mice. Data are mean ± s.e.m. *P* values were calculated using unpaired two-sided Student's *t*-test with Welch's correction. N.D., not detected.

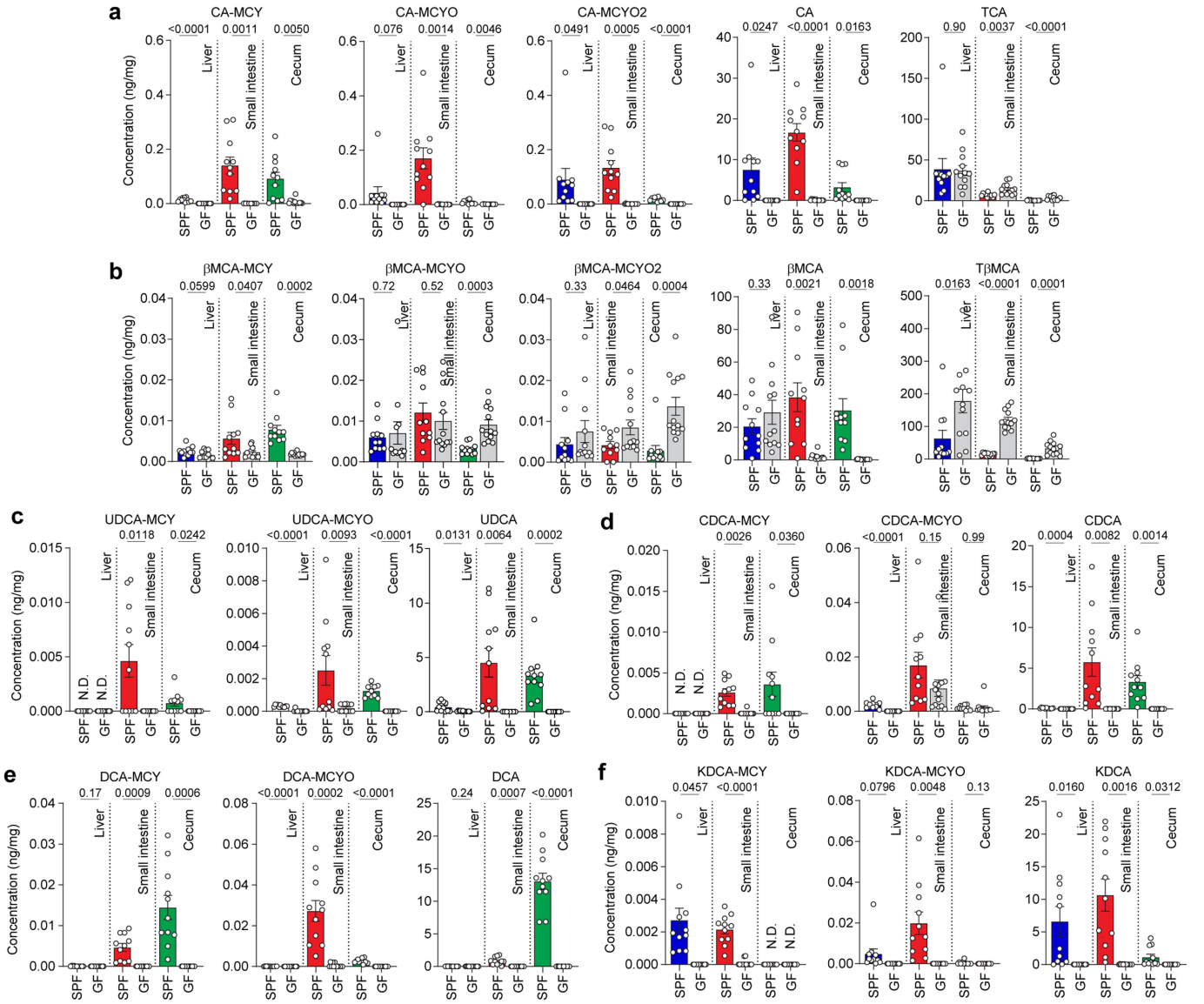

Extended Data Fig. 6 | Abundances of BA-MCY conjugates in different tissues. a,**b**, Abundances of CA-MCY conjugates, TCA and CA (**a**), and βMCA-MCY conjugates, TβMCA and βMCA (**b**) in liver, small intestine, and cecum of SPF (n = 11) and GF (n = 12 for liver and n = 13 for small intestine and cecum) mice. Data are mean ± s.e.m. **c**–**f**, Abundances of UDCA-MCY conjugates and UDCA (**c**), CDCA-MCY conjugates and CDCA (**d**), DCA-MCY conjugates and DCA (**e**), and 7-KDCA-MCY conjugates and 7-KDCA (**f**) in liver, small intestine, and cecum of SPF (n = 11) and GF (n = 12 for liver and n = 13 for small intestine and cecum) mice. Data are mean ± s.e.m. *P* values were calculated using unpaired two-sided Student's *t*-test with Welch's correction. N.D., not detected.

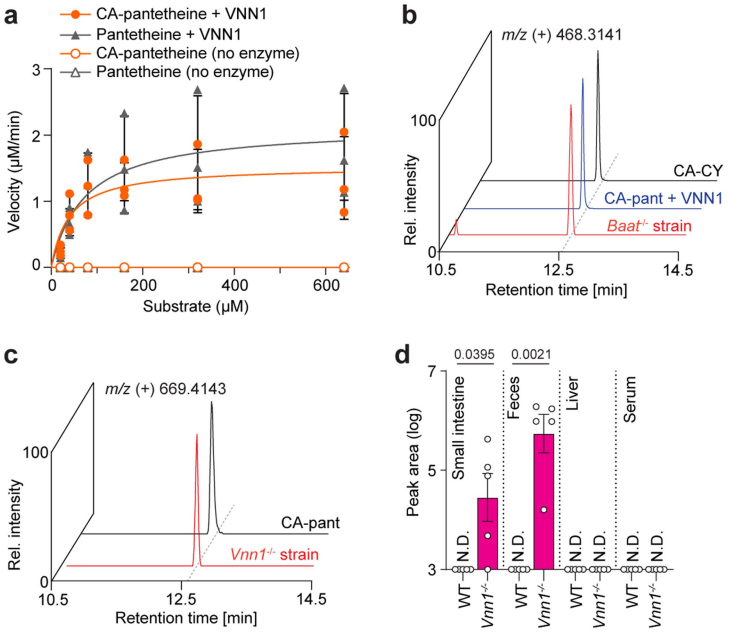

Extended Data Fig. 7 | The role of VNN1 in production of BA-MCY conjugates. **a**, Steady-state kinetic analysis of CA-pant and pantetheine hydrolysis catalyzed by recombinant human VNN1 (ΔN490aa truncated) revealed both reactions follow saturation kinetics. The steady-state kinetic parameters K_m and V_{max} are determined by HPLC-HRMS for pantothenic acid formation to be 39.78 ± 20.31 μM and 1.53 ± 0.20 min^{-1} for CA-pant, and 74.07 ± 41.52 μM and 2.13 ± 0.37 min^{-1} for pantetheine. The reaction mixtures contain 0.01 μM VNN1. Number of independent assays using the same batch of enzyme (n = 3). Data are mean ± s.d. **b**, EICs of CA-CY in ileum of *Baat*$^{-/-}$ mice, extracts of in vitro reaction of VNN1 hydrolyses CA-pantetheine, and comparison with a synthetic standard analyzed in ESI + . **c**, EICs of CA-pant in small intestine of *Vnn1*$^{-/-}$ mice and comparison with a synthetic standard analyzed in ESI + . **d**, Relative abundances of CA-pant in small intestine, feces, liver, and serum of WT (n = 5) and *Vnn1*$^{-/-}$ (n = 5) mice. Data are mean ± s.e.m. *P* values were calculated using unpaired two-sided Student's *t*-test with Welch's correction. N.D., not detected.

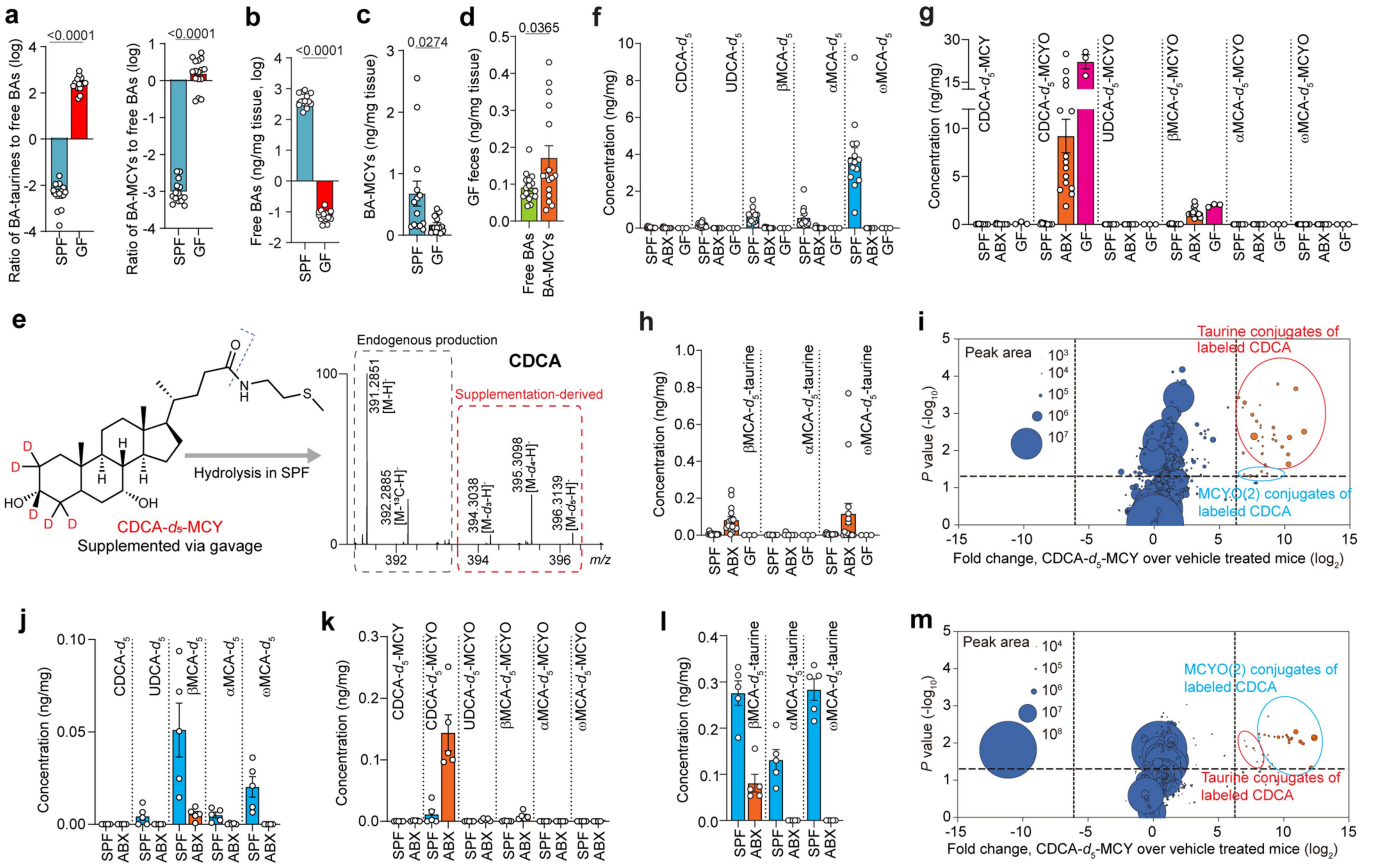

Extended Data Fig. 8 | Microbial deconjugation of BA-MCYs in SPF, GF, and ABX mice. a, Ratio of total BA-taurine or BA-MCY conjugates to corresponding free BAs in feces of SPF (n = 14) and GF (n = 16) mice. Data are mean ± s.e.m. *P* values were calculated using unpaired two-sided Student's *t*-test with Welch's correction. **b**,**c**, Total amounts of free BAs (**b**) or BA-MCY conjugates (**c**) in feces of SPF (n = 14) and GF (n = 16) mice. Data are mean ± s.e.m. *P* values were calculated using unpaired two-sided Student's *t*-test with Welch's correction. **d**, Total amounts of free BAs and BA-MCY conjugates in feces of GF (n = 16) mice. Data are mean ± s.e.m. *P* values were calculated using paired two-sided Student's *t*-test. **e**, HRMS analysis of feces of mice fed CDCA-d_5-MCY revealed deconjugation of supplemented CDCA-d_5-MCY, represented by peaks in the CDCA mass spectrum highlighted in red. Endogenously produced CDCA can be distinguished, highlighted in green. CA remained unlabeled. **f**–**h**, Total amounts of labeled free BAs (**f**), BA-MCY conjugates (**g**), and BA-taurine conjugates (**h**) in feces of SPF (n = 14), ABX (n = 15), and GF (n = 3) mice administered CDCA-d_5-MCY. **i**, Volcano plot of differential metabolites detected in liver of SPF mice administered control (corn oil) (n = 4) or CDCA-d_5-MCY (n = 5). Bubble sizes reflect peak areas. See Supplementary Table 4 for compounds derived from supplemented CDCA-d_5-MCY. *P* values were calculated using unpaired two-sided Student's *t*-test. **j**–**l**, Total amounts of labeled free BAs (**j**), BA-MCY conjugates (**k**), and BA-taurine conjugates (**l**) in liver of SPF (n = 5) and ABX (n = 5) mice administered CDCA-d_5-MCY. **m**, Volcano plot of differential metabolites detected in liver of ABX mice administered control (corn oil) (n = 4) or CDCA-d_5-MCY (n = 5). Bubble sizes reflect peak areas. See Supplementary Table 4 for compounds derived from supplemented CDCA-d_5-MCY. *P* values were calculated using unpaired two-sided Student's *t*-test.

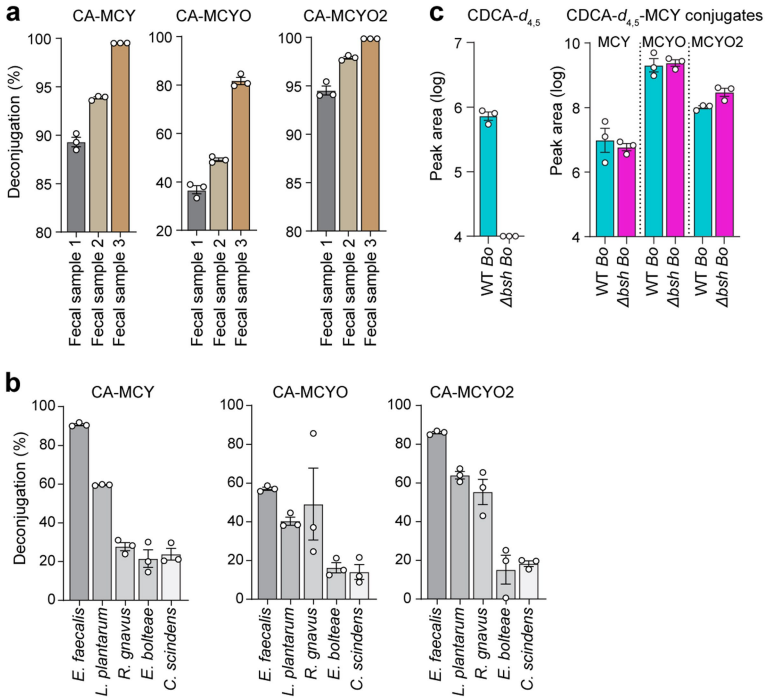

Extended Data Fig. 9 | Microbial deconjugation of BA-MCYs in vitro and gnotobiotic mice. a,b, Deconjugation of CA-MCY conjugates in fecal suspensions obtained from SPF mice (**a**) (n = 3) and cultured gut bacteria (**b**) (n = 3). **c**, Relative abundances of CDCA-d_5-MCY conjugates and corresponding free BA in feces of GF monocolonized with WT (n = 3) or BSH-deficient *B. ovatus* (n = 3) (WT *Bo* and *Δbsh Bo*, respectively). Data are mean ± s.e.m. *P* values were calculated using unpaired two-sided Student's *t*-test with Welch's correction.

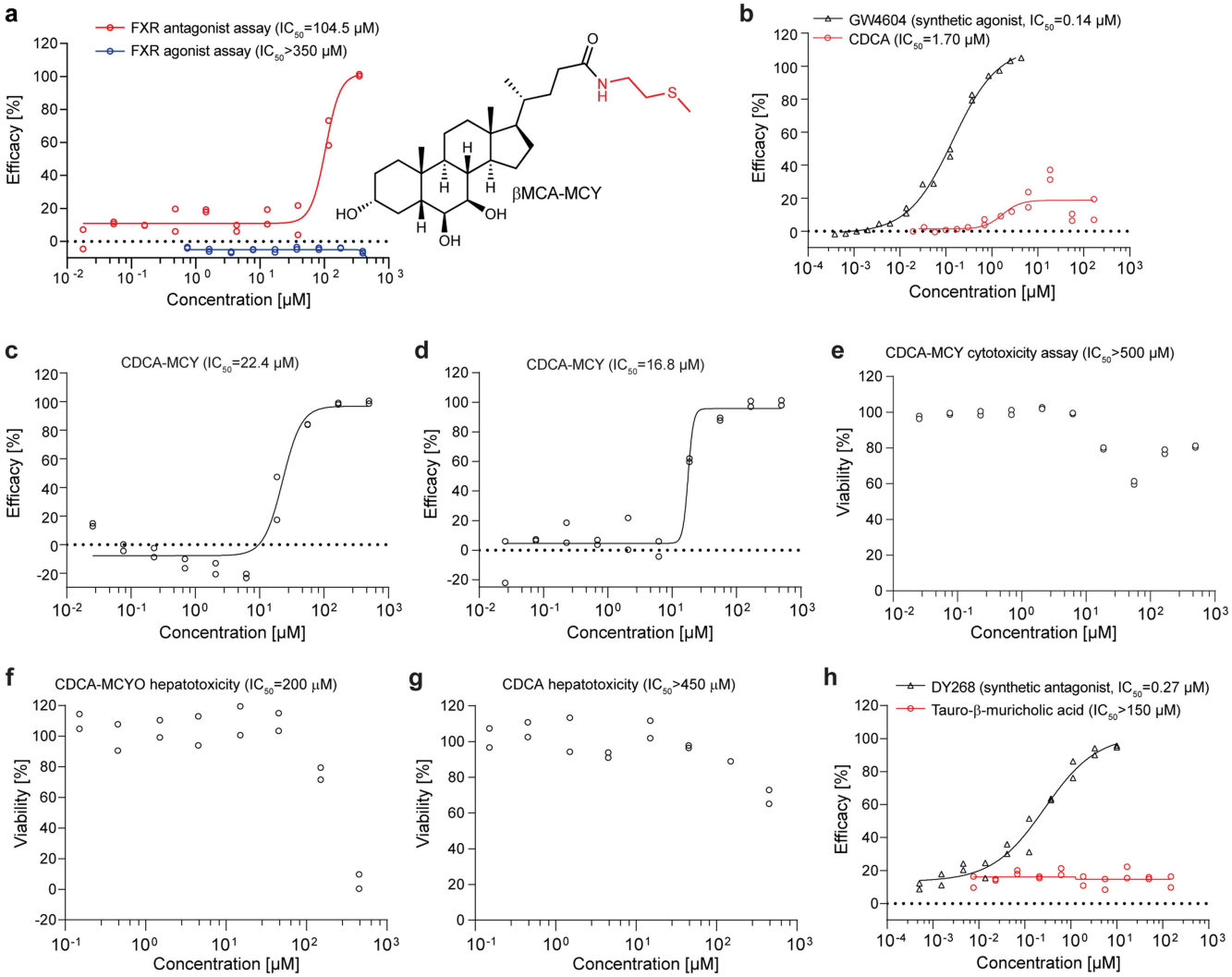

Extended Data Fig. 10 | FXR-related activity of known ligands and BA-MCYs. **a**, βMCA-MCY was tested against a cell-based protein-protein interaction assays in both agonist and antagonist modes. βMCA-MCY showed strong FXR antagonistic effects to GW4604-mediated activation of FXR. βMCA-MCY showed no FXR agonistic effects in the assay. Assays were performed in duplicate for each concentration. **b**, FXR agonistic effect of CDCA as measured in the protein-protein interaction assays. Data were normalized to the maximal and minimal response observed in the presence of control compound (GW4064) and vehicle (DMSO), respectively. Assays were performed in duplicate for each concentration. **c**,**d**, CDCA-MCY showed FXR antagonistic effects to obeticholic acid (25 μM) (**c**) or CDCA (25 μM) (**d**) mediated activation of FXR. Data were normalized to the maximal and minimal response observed in the presence of control compound (DY268) and vehicle (DMSO), respectively. Assays were performed in duplicate for each concentration. **e**–**g**, Cytotoxicity assays for CDCA-MCY (**e**), CDCA-MCYO (**f**), and CDCA (**g**) in a cell-based assay on human primary hepatocytes. Assays were performed in duplicate for each concentration. **h**, TβMCA did not show FXR antagonistic effects in protein-protein interaction assays at the tested concentrations. DY268 a synthetic FXR antagonist was used as a positive control. Data were normalized to the maximal and minimal response observed in the presence of control compound (DY268) and vehicle (DMSO), respectively. Assays were performed in duplicate for each concentration.

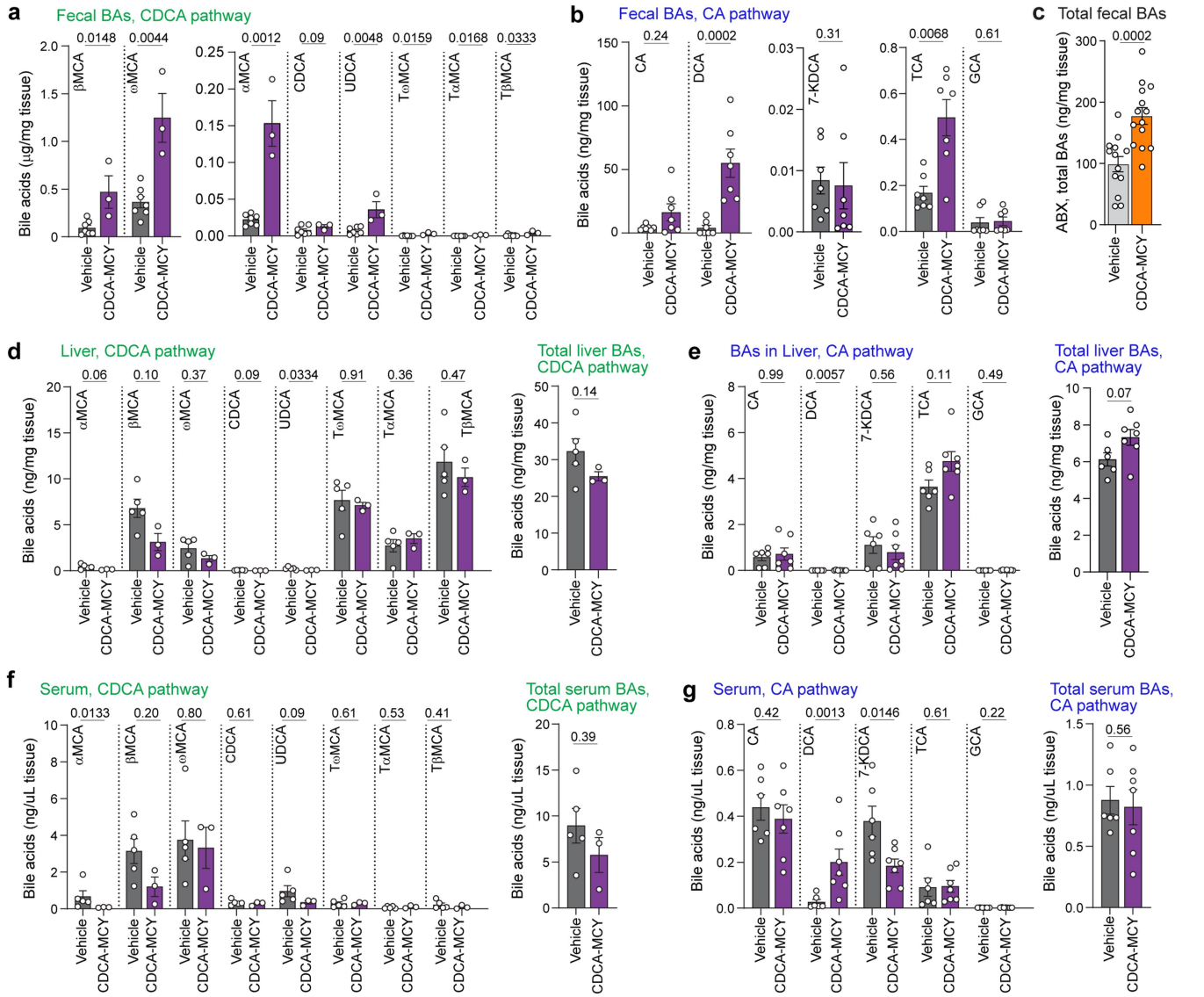

Extended Data Fig. 11 | Regulation of BA biosynthesis by BA-MCYs in vivo. **a**,**b**, Abundances of endogenously produced BAs in feces of mice administered CDCA-MCY or CDCA-d_5-MCY daily for 14 days. Shown are individual amounts of CDCA-derived BAs (**a**) and CA-derived BAs (**b**) in feces. Data are mean ± s.e.m. with control (corn oil) (n = 7) and CDCA-MCY fed mice (n = 7 for CDCA-derived pathway and n = 3 for CA-derived pathway). *P* values were calculated using unpaired two-sided Student's *t*-test with Welch's correction. **c**, Total endogenously produced BAs in feces of ABX mice administered CDCA-d_5-MCY. Shown are total amounts of BAs (n = 13 for control and n = 14 for CDCA-MCY fed mice). Data are mean ± s.e.m. *P* values were calculated using unpaired two-sided Student's *t*-test with Welch's correction. **d**,**e**, Abundances of CDCA-derived BAs (**d**) and CA-derived BAs (**e**) in liver of mice administered CDCA-MCY or CDCA-d_5-MCY daily for 14 days. Data are mean ± s.e.m. with control (corn oil) (n = 6) and CDCA-MCY fed mice (n = 3 for CDCA-derived pathway and n = 7 for CA-derived pathway). *P* values were calculated using unpaired two-sided Student's *t*-test with Welch's correction. **f**,**g**, Abundances of CDCA-derived BAs (**f**) and CA-derived BAs (**g**) in serum of mice administered CDCA-MCY or CDCA-d_5-MCY daily for 14 days. Data are mean ± s.e.m. with control (corn oil) (n = 6) and CDCA-MCY fed mice (n = 3 for CDCA-derived pathway and n = 7 for CA-derived pathway). *P* values were calculated using unpaired two-sided Student's *t*-test with Welch's correction.

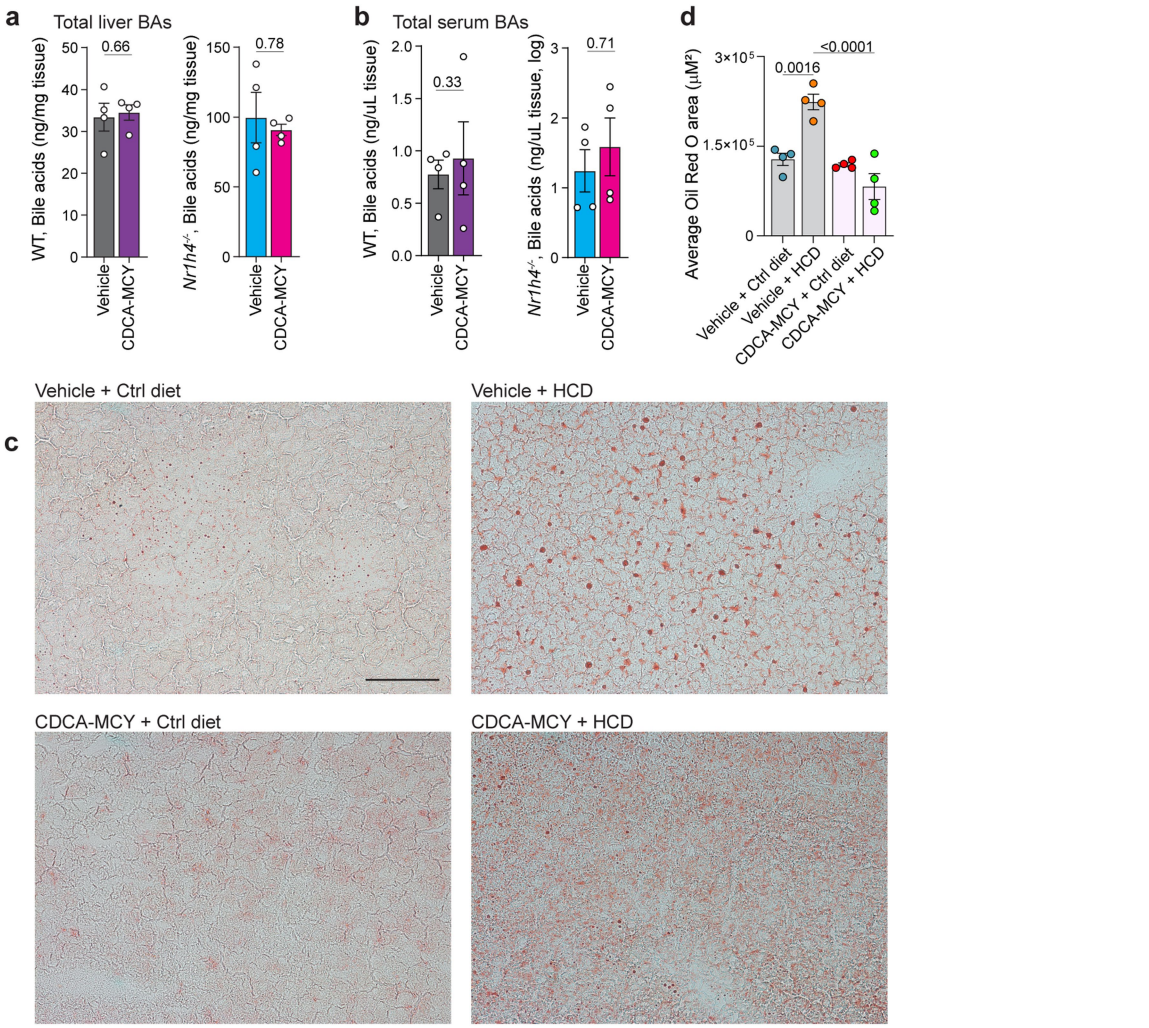

Extended Data Fig. 12 | FXR-related activity of BA-MCYs in vivo. **a**,**b**, Abundances of total BAs in liver (**a**) and serum (**b**) of WT and *Nr1h4*$^{-/-}$ mice administered CDCA-d_5-MCY daily for 14 days. Data are mean ± s.e.m. with control (corn oil) (n = 4) and CDCA-d_5-MCY fed mice (n = 4). *P* values were calculated using unpaired two-sided Student's *t*-test with Welch's correction. **c**, Representative photomicrographs of oil red O staining of liver sections of mice treated with the indicated conditions. Mice were fed control (n = 4 for vehicle and n = 4 for CDCA-MCY) or high cholesterol diet (HCD) (n = 4 for vehicle and n = 4 for CDCA-MCY). CDCA-MCY was delivered by oral gavage at a rate of 5 mg/kg body weight per day for two weeks. Scale bar, 100 µm. **d**, Average measured oil red O area of liver sections of mice in **c**. Data are mean ± s.e.m. *P* values were calculated using one-way ANOVA with Tukey's correction.

nature portfolio

Corresponding author(s): Frank C. Schroeder and David Artis

Last updated by author(s): Oct 29, 2024

Reporting Summary

Nature Portfolio wishes to improve the reproducibility of the work that we publish. This form provides structure for consistency and transparency in reporting. For further information on Nature Portfolio policies, see our Editorial Policies and the Editorial Policy Checklist.

Statistics

For all statistical analyses, confirm that the following items are present in the figure legend, table legend, main text, or Methods section.

n/a	Confirmed	
☐	☒	The exact sample size (*n*) for each experimental group/condition, given as a discrete number and unit of measurement
☐	☒	A statement on whether measurements were taken from distinct samples or whether the same sample was measured repeatedly
☐	☒	The statistical test(s) used AND whether they are one- or two-sided *Only common tests should be described solely by name; describe more complex techniques in the Methods section.*
☐	☒	A description of all covariates tested
☐	☒	A description of any assumptions or corrections, such as tests of normality and adjustment for multiple comparisons
☐	☒	A full description of the statistical parameters including central tendency (e.g. means) or other basic estimates (e.g. regression coefficient) AND variation (e.g. standard deviation) or associated estimates of uncertainty (e.g. confidence intervals)
☐	☒	For null hypothesis testing, the test statistic (e.g. *F*, *t*, *r*) with confidence intervals, effect sizes, degrees of freedom and *P* value noted *Give P values as exact values whenever suitable.*
☒	☐	For Bayesian analysis, information on the choice of priors and Markov chain Monte Carlo settings
☒	☐	For hierarchical and complex designs, identification of the appropriate level for tests and full reporting of outcomes
☒	☐	Estimates of effect sizes (e.g. Cohen's *d*, Pearson's *r*), indicating how they were calculated

Our web collection on statistics for biologists contains articles on many of the points above.

Software and code

Policy information about availability of computer code

Data collection	LC-MS data were collected using Thermo Scientific Xcalibur software version 4.1.31.9; QuantStudio Real-Time PCR software v1.0 was used to collect real-time PCR data.
Data analysis	LC-MS data were converted using MSConvert (ProteoWizard v3.0.18250-994311be0), then analyzed using Metaboseek software (v0.9.7). Quantification was performed via integration in Xcalibur 4.1 QualBrowser (v4.1.31.9 ,Thermo Scientific). A MS2 molecular network was created using Metaboseek (v0.9.7) and visualized in Cytoscape (v3.9.1). MS Excel (v2112) and Graphpad PRISM (v10.2.0) were used to plot. All statistical analysis were performed with GraphPad Prism version 10.2.0 or Metaboseek version 0.9.7. NMR spectra were processed and baseline corrected using MestreLab MNOVA (v14.2.1-27684) software packages. The custom Fiji script used for the analysis of liver lipid accumulation imaging is available at https://github.com/cnp9004/Fiji-ORO-macro.

For manuscripts utilizing custom algorithms or software that are central to the research but not yet described in published literature, software must be made available to editors and reviewers. We strongly encourage code deposition in a community repository (e.g. GitHub). See the Nature Portfolio guidelines for submitting code & software for further information.

Data

Policy information about availability of data

All manuscripts must include a data availability statement. This statement should provide the following information, where applicable:

- Accession codes, unique identifiers, or web links for publicly available datasets
- A description of any restrictions on data availability
- For clinical datasets or third party data, please ensure that the statement adheres to our policy

Raw sequencing reads were uploaded to the Sequence Read Archive (SRA), and MS data for all mouse metabolome samples analyzed in this study were uploaded to the GNPS Web site (massive.ucsd.edu) under MassIVE ID number MSV000090974 and will be publicly available as of the date of publication.

Human research participants

Policy information about studies involving human research participants and Sex and Gender in Research.

Reporting on sex and gender	For FMT studies, the donors include 2 females and one male (self-reported). For human serum samples, participants were 12 females and 8 males. However, gender- or sex-based analyses were not performed since sample sizes were small and the results from male and female donors are similar.
Population characteristics	For human serum samples, all participants were between the ages of 18 and 35, weighed at least 110 pounds (50 kg), and had a body mass index (BMI) between 17.0 and 27.5. For FMT studies, all participants are between ages of 27 and 51.
Recruitment	Donors were defined healthy based on the absence of any gastrointestinal inflammation or metabolic syndrome including diabetes and obesity (BMI>30) during the collection of samples.
Ethics oversight	For human serum samples, the original study protocol was approved by the Duke Health Institutional Review Board (IRB) at Duke University under protocol number Pro00093322, and registered on ClinicalTrials.gov, with the identified number NCT04055246. Informed consent was obtained from all participants. For FMT studies, the study protocol was approved by the Institutional Review Board at Weill Cornell Medicine.

Note that full information on the approval of the study protocol must also be provided in the manuscript.

Field-specific reporting

Please select the one below that is the best fit for your research. If you are not sure, read the appropriate sections before making your selection.

☒ Life sciences ☐ Behavioural & social sciences ☐ Ecological, evolutionary & environmental sciences

For a reference copy of the document with all sections, see nature.com/documents/nr-reporting-summary-flat.pdf

Life sciences study design

All studies must disclose on these points even when the disclosure is negative.

Sample size	No sample size calculations were performed. Sample sizes were selected based on reasonable replication and prior experience with similar assays which provided conclusive evidence of sufficient sample sizes, see e.g., PMID: 38506708 and PMID: 31645720 for examples.
Data exclusions	No data excluded for any of the experiments in the manuscripts.
Replication	Experiments were independently replicated as indicated; three or more times in most cases. Replicates were biologically independent, unless indicated otherwise. All attempts at replication were successful.
Randomization	Mice were randomly assigned to experimental groups at the beginning of dietary or metabolite treatments. Age and sex were matched between experimental groups. All human samples were assigned to and tested for every experimental groups.
Blinding	For all animal experiments, investigators were not blinded to the experimental groups given different diets or housing conditions were required. All human samples were assigned to and tested for every experimental groups and therefore blinding was not applicable. For the oil red O staining and quantification, images were acquired and analyzed by an individual blinded to the treatment groups. Investigators were blinded during tissue extraction and subsequent sample preparation for metabolomics.

Reporting for specific materials, systems and methods

We require information from authors about some types of materials, experimental systems and methods used in many studies. Here, indicate whether each material, system or method listed is relevant to your study. If you are not sure if a list item applies to your research, read the appropriate section before selecting a response.

Materials & experimental systems

n/a	Involved in the study
☐	☒ Antibodies
☐	☒ Eukaryotic cell lines
☒	☐ Palaeontology and archaeology
☐	☒ Animals and other organisms
☒	☐ Clinical data
☒	☐ Dual use research of concern

Methods

n/a	Involved in the study
☒	☐ ChIP-seq
☒	☐ Flow cytometry
☒	☐ MRI-based neuroimaging

Antibodies

Antibodies used	FGF15 ELISA was performed using the mouse Fgf15 ELISA Kit (LSBio) as per the manufacturer's protocol.
Validation	The quality of the ELISA kit containing mouse Fgf15 antibody is tested and guaranteed by the manufacturer.

Eukaryotic cell lines

Policy information about cell lines and Sex and Gender in Research

Cell line source(s)	CHO-K1 from Eurofins DiscoverX.
Authentication	The cell lines were not authenticated.
Mycoplasma contamination	All cell lines tested negative for mycoplasma by Eurofins DiscoverX.
Commonly misidentified lines (See ICLAC register)	None.

Animals and other research organisms

Policy information about studies involving animals; ARRIVE guidelines recommended for reporting animal research, and Sex and Gender in Research

Laboratory animals	C57BL/6 (Jax, 000664) and Nr1h4-/- (Jax, 007214) mice were originally purchased from The Jackson Laboratories and bred at Weill Cornell Medicine (WCM). Vnn1-/- mice were bred at the Yale School of Medicine (gift of Dr. Phillipe Nasquet (CIML, France) and Dr. Ruslan Medzhitov (Yale University, USA). GF C57BL/6J mice were bred and housed in flexible PVC isolators (Park Bioservices) at WCM. Gnotobiotic mice were maintained in Sentry sealed positive pressure cages (SPP, Allentown) for the duration of the experiments. All other mice were maintained under specific pathogen-free condition. All mice used were between 6 and 12 weeks old, age- and sex-matched for each experiment, maintained on a 12-h light-dark cycle, an average ambient temperature of 21 °C, an average humidity of 48%, and were provided food and water ad libitum. When studying the effects of dietary fiber, mice were given an inulin fiber diet (D16052309, Research Diets, Inc.) supplemented with 30% fiber (26% 412 inulin and 4% cellulose) or a calorie-matched control diet (D12450J-1.5, Research Diets, Inc.) containing 4.7% cellulose. The duration of the fiber dietary intervention was two weeks unless otherwise stated. For the experimental model of hypercholesteremia, mice were given a high cholesterol diet (C23041301, Research Diets, Inc.) supplemented with 1% cholesterol, or standard mouse chow. The duration of the high cholesterol dietary intervention was four weeks.
Wild animals	No wild animals were used in the study.
Reporting on sex	Equal numbers of male and female mice were used for all metabolomics experiments and age and sex-matched animals were used for functional experiments with metabolites.
Field-collected samples	No field collected samples were used in the study.
Ethics oversight	All protocols were approved by the Weill Cornell Medicine Institutional Animal Care and Use Committees (IACUC), and all mice were used in accordance of governmental and institutional guidelines for animal welfare.

Note that full information on the approval of the study protocol must also be provided in the manuscript.